

## MACHO Alert 95–30 : First Real–Time Observation of Extended Source Effects in Gravitational Microlensing

C. Alcock<sup>1,2</sup>, W.H. Allen<sup>3</sup>, R.A. Allsman<sup>4</sup>, D. Alves<sup>1,5,27</sup>, T.S. Axelrod<sup>6</sup>, T.S. Banks<sup>7</sup>,  
S.F. Beaulieu<sup>8</sup>, A.C. Becker<sup>2,9</sup>, R.H. Becker<sup>1,5</sup>, D.P. Bennett<sup>1,2,10</sup>, I.A. Bond<sup>11</sup>, B.S. Carter<sup>3</sup>,  
K.H. Cook<sup>1</sup>, R.J. Dodd<sup>3</sup>, K.C. Freeman<sup>6</sup>, M. Gregg<sup>1,5</sup>, K. Griest<sup>2,12</sup>, J.B. Hearnshaw<sup>13</sup>,  
A. Heller<sup>14</sup>, M. Honda<sup>15</sup>, J. Jugaku<sup>16</sup>, S. Kabe<sup>17</sup>, S. Kaspi<sup>14</sup>, P.M. Kilmartin<sup>13,18</sup>, A. Kitamura<sup>11</sup>,  
O. Kovo<sup>14</sup>, M.J. Lehner<sup>2,12</sup>, T.E. Love<sup>13,18</sup>, D. Maoz<sup>14</sup>, S.L. Marshall<sup>1</sup>, Y. Matsubara<sup>11</sup>,  
D. Minniti<sup>1</sup>, M. Miyamoto<sup>19</sup>, Y. Muraki<sup>11</sup>, T. Nakamura<sup>20</sup>, B.A. Peterson<sup>6</sup>, M.R. Pratt<sup>2,9,21</sup>,  
P.J. Quinn<sup>22</sup>, I. N. Reid<sup>23</sup>, M. Reid<sup>7</sup>, D. Reiss<sup>9</sup>, A. Retter<sup>14</sup>, A.W. Rodgers<sup>6</sup>, W. L. W. Sargent<sup>23</sup>,  
H. Sato<sup>20</sup>, M. Sekiguchi<sup>19</sup>, P.B. Stetson<sup>24</sup>, C.W. Stubbs<sup>2,6,9,21</sup>, D.J. Sullivan<sup>7</sup>, W. Sutherland<sup>25</sup>,  
A. Tomaney<sup>9</sup>, T. Vandehei<sup>12</sup>, Y. Watase<sup>17</sup>, D.L. Welch<sup>26</sup>, T. Yanagisawa<sup>11</sup>, M. Yoshizawa<sup>20</sup>,

and

P.C.M. Yock<sup>18</sup>

(The MACHO and GMAN Collaborations)

---

<sup>1</sup>Lawrence Livermore National Laboratory, Livermore, CA 94550

<sup>2</sup>Center for Particle Astrophysics, University of California, Berkeley, CA 94720

<sup>3</sup>Carter National Observatory, Wellington, New Zealand

<sup>4</sup>Supercomputing Facility, Australian National University, Canberra, ACT 0200, Australia

<sup>5</sup>Department of Physics, University of California, Davis, CA 95616

<sup>6</sup>Mt. Stromlo and Siding Spring Observatories, Australian National University, Weston, ACT 2611, Australia

<sup>7</sup>Department of Physics, Victoria University, Wellington, New Zealand

<sup>8</sup>Space Telescope Science Institute, San Martin Drive 3700, Baltimore, MN 21218

<sup>9</sup>Departments of Astronomy and Physics, University of Washington, Seattle, WA 98195

<sup>10</sup>Department of Physics, University of Notre Dame, Notre Dame, IN 46556

<sup>11</sup>Solar–Terrestrial Environment Laboratory, Nagoya University, Nagoya 464-01, Japan

<sup>12</sup>Department of Physics, University of California, San Diego, CA 92093

<sup>13</sup>Department of Physics and Astronomy, University of Canterbury, Christchurch, New Zealand

<sup>14</sup>School of Physics & Astronomy and Wise Observatory, Tel-Aviv University, Tel-Aviv 69978, Israel

<sup>15</sup>Institute for Cosmic Ray Research, University of Tokyo, Tokyo 188, Japan

<sup>16</sup>Research Institute of Civilization, Tokai University, Hiratsuka 259-12, Japan

<sup>17</sup>National Laboratory of High Energy Physics (KEK), Tsukuba 305, Japan

<sup>18</sup>Faculty of Science, University of Auckland, Auckland, New Zealand

<sup>19</sup>National Astronomical Observatory, Mitaka, Tokyo 181, Japan

<sup>20</sup>Department of Physics, Kyoto University, Kyoto 606, Japan

<sup>21</sup>Department of Physics, University of California, Santa Barbara, CA 93106

<sup>22</sup>European Southern Observatory, Karl-Schwarzschild Str. 2, D-85748, Garching, Germany

<sup>23</sup>Astronomy Department 105-24, Caltech, Pasadena, CA 91125

<sup>24</sup>Dominion Astrophysical Observatory, 5071 West Saanich Road, RR 5, Victoria, BC V8X 4M6, Canada

<sup>25</sup>Department of Physics, University of Oxford, Oxford OX1 3RH, U.K.

<sup>26</sup>Departments of Physics and Astronomy, McMaster University, Hamilton, Ontario Canada L8S 4M1

<sup>27</sup>Visiting astronomer, Cerro Tololo Inter-American Observatory

## ABSTRACT

We present analysis of MACHO Alert 95–30, a dramatic gravitational microlensing event towards the Galactic bulge whose peak magnification departs significantly from the standard point–source microlensing model. Alert 95–30 was observed in real–time by the Global Microlensing Alert Network (GMAN), which obtained densely sampled photometric and spectroscopic data throughout the event. We interpret the light–curve “fine structure” as indicating transit of the lens across the extended face of the source star. This signifies resolution of a star several kpc distant.

We find a lens angular impact parameter  $\theta_{min}/\theta_{source} = 0.715 \pm 0.003$ . This information, along with the radius and distance of the source, provides an additional constraint on the lensing system. Spectroscopic and photometric data indicate the source is an M4 III star of radius  $61 \pm 12 R_{\odot}$ , located on the far side of the bulge at  $\sim 9$  kpc. We derive a lens angular velocity, relative to the source, of  $21.5 \pm 4.9 \text{ km s}^{-1} \text{ kpc}^{-1}$ , where the error is dominated by uncertainty in the source radius. Likelihood analysis yields a median lens mass of  $0.67_{-0.46}^{+2.53} M_{\odot}$ , located with 80% probability in the Galactic bulge at a distance of  $6.93_{-2.25}^{+1.56}$  kpc. If the lens is a main–sequence star, we can include constraints on the lens luminosity. This modifies our estimates to  $M_{lens} = 0.53_{-0.35}^{+0.52} M_{\odot}$  and  $D_{lens} = 6.57_{-2.25}^{+0.99}$  kpc.

Spectra taken during the event show that the absorption line equivalent widths of  $H\alpha$  and the TiO bands near  $6700\text{\AA}$  vary, as predicted for microlensing of an extended source. This is most likely due to center–to–limb variation in the stellar spectral lines. The observed spectral changes further support our microlensing interpretation. These data demonstrate the feasibility of using microlensing limb crossings as a tool to probe stellar atmospheres directly.

*Subject headings:* dark matter - gravitational lensing - stars: low-mass, brown dwarfs - stars: late-type - stars: atmospheres

## 1. Introduction

The MACHO collaboration is undertaking an extensive search for gravitational microlensing by objects in the Galactic halo, bulge, and disk. Nightly observations of millions of stars in the Large Magellanic Cloud (LMC) and Galactic bulge have yielded a total of 8 LMC (Alcock et al. 1996c) and more than 120 bulge events (Alcock et al. 1995a; Alcock et al. 1996b; MACHO Alert system <sup>1</sup>). Similar observations are being undertaken towards the LMC by EROS (Renault et al. 1996) with 2 reported events, as well as towards the bulge by OGLE (Paczynski et al. 1995) with 18 reported events and DUO (Alard et al. 1995) with some 10 reported events. New efforts to detect the microlensing of unresolved stars in M31 are being undertaken by the AGAPE (Gondolo et al. 1996) and VATT/Columbia (Crotts 1996) collaborations. Reviews of the field of gravitational microlensing are presented in Gould (1996) and Paczynski (1996).

Statistical analysis of an ensemble of microlensing events provides a useful discriminant between Galactic structure models. Two years of observations towards the LMC yield a microlensing optical depth representing approximately 50% of a “standard” Galactic halo comprised entirely of massive compact halo objects (Alcock et al. 1996c). Similar analysis of Galactic bulge data, as reported by MACHO and OGLE (Alcock et al. 1996b; Udalski et al. 1994a), indicate an optical depth a factor of  $\sim 3$  larger than predicted by axisymmetric Galactic models (e.g. Griest et al. 1991; Paczynski 1991). Consistent Galactic models have recently been constructed which include a Galactic bar viewed nearly end-on (Kiraga & Paczynski 1994; Zhao et al. 1996; Binney et al. 1996). However, it is difficult to identify clearly a lensing population because the mass, velocity, and distance of each lens are not uniquely determined in the standard microlensing solution.

Gravitational microlensing is characterized by the transient, achromatic brightening of a background star due to gravitational deflection of its light by a massive “lens” passing near our line of sight to the source. This results in the distortion of the source disk into multiple (unresolved) images whose total brightness is greater than that of the original source brightness. Given the assumptions of a point-mass lens, point source, and unaccelerated motion, the source magnification  $A(t)$  is of the simple form

$$A(t) = \frac{u^2 + 2}{u\sqrt{u^2 + 4}}, \quad (1)$$

where  $u(t) = \sqrt{u_{min}^2 + (2(t - t_0)/\hat{t})^2}$ .

These equations describe the event’s “light-curve” as a function of time.  $A(t)$  is the observed source magnification,  $\hat{t} = 2R_E/v_{\perp}$  is the characteristic event timescale, where  $v_{\perp}$  is the transverse

---

<sup>1</sup>Current information on the MACHO Collaboration’s Alert events is maintained at the WWW site <http://darkstar.astro.washington.edu>.

velocity of the lens, and

$$R_E^2 \equiv \frac{4GM}{c^2} x(1-x)L \quad (2)$$

is a conveniently defined distance scale in the lens plane (the lens’s Einstein radius).  $M$  is the mass of the deflector, and  $x$  is the ratio of the observer–lens to observer–source ( $L$ ) distances. The equation for  $u(t)$  describes the impact parameter of the lens, scaled by  $R_E$ , as it passes near the source, and  $t_0$  and  $u_{\min}$  are the values of  $t$  and  $u$  at peak magnification.

Fitting a normal microlensing event provides only one parameter,  $\hat{t}$ , containing information about the lens. However,  $\hat{t}$  is a function of the three unknowns  $M$ ,  $x$  and  $v_{\perp}$ . (Strictly speaking, the source distance  $L$  is also unknown, but the uncertainty in  $L$  is typically much smaller than that in  $x$ , so it is simpler to treat  $L$  as known). This indicates a continuum of event parameters which can conspire to produce similar duration microlensing events.

## 2. Light–Curve Fine Structure and Extended Source Effects

In instances where the standard approximations break down, light–curve “fine structure” describes deviations from the standard model whose nature may break this degeneracy. Important microlensing events in this regime include the detection of binary microlensing (Udalski et al. 1994b; Pratt et al. 1995; Alard, Mao, & Guibert 1995; Alcock et al. 1996d), and the observation of parallax in a gravitational microlensing event (Alcock et al. 1995b). An exciting possibility is the detection of short timescale deviations in an event light–curve due to the presence of planets in the “lensing zone” of the microlensing system (Mao & Paczyński 1991; Gould & Loeb 1992; Bennett & Rhie 1996).

The effects of extended source size may also become apparent in the limit of a large source, high magnification event, where the lens impact parameter is of the order of the projected source radius (Gould 1994; Nemiroff & Wickramasinghe 1994; Witt & Mao 1994; Peng 1997). In this situation, an extra parameter is included in the microlensing solution,  $u_* = xR_*/R_E$ . Here  $R_*$  is the radius of the source star, and  $u_*$  describes its projection into the lens plane, scaled by  $R_E$ . Due to its geometric nature,  $u(t)$  is not changed by this parameterization. An analytic solution for  $A(t)$  in this limit is presented in Witt & Mao (1994).

Fitting the light–curve with the extra parameter  $u_*$  provides a second constraint equation for the three lens parameters - the angular size of the source in terms of the lens’s Einstein radius. If we estimate the linear radius and distance of the source star from photometry and spectroscopy, we have an estimate of the lens proper motion relative to the source, which leads to a unique mass–distance relation for the lens. Such a situation is rare, and would be expected in only  $\sim 5\%$  of events towards the galactic bulge (Gould & Welch 1996).

To account for limb-darkening of the source, an appropriate limb-darkening law and coefficients must be determined for the source star. The magnification is then integrated over the face of the star, properly weighted by the brightness profile. The limb-darkening law we will choose is of the form (e.g. Claret, Díaz-Cordovés, & Giménez (1995))

$$I_{\lambda}(\mu)/I_{\lambda}(1) = 1 - a(1 - \mu) - b(1 - \mu)^2. \quad (3)$$

Here  $\mu$  is the cosine of the angle between the observer’s line of sight and the emerging stellar radiation, and  $a$  and  $b$  are model parameters dependent primarily upon the effective temperature and surface gravity of the star.

### 3. Global Microlensing Alert Network (GMAN)

To provide both the temporal and photometric resolution necessary to distinguish light-curve “fine structure”, coordinated follow-up observations are being undertaken through the Global Microlensing Alert Network (GMAN) (Pratt et al. 1995; Alcock et al. 1996a), as well as the PLANET collaboration (Albrow et al. 1997).

GMAN utilizes telescope resources at Cerro Tololo Inter-American Observatory <sup>2</sup> (CTIO), Mount John University Observatory (MJUO), University of Toronto Southern Observatory (UTSO), and Wise Observatory which respond nightly to the dynamic status of ongoing microlensing events (see Table 1). Observations from MJUO are carried out by the MOA collaboration of Japan and New Zealand, which is undertaking a general survey of microlensing events towards the Magellanic Clouds and the Galactic bulge (Abe et al. 1997). The observational flexibility available at these locations provided nearly continuous coverage of this event.

Microlensing follow-up images are automatically processed on site. Photometry is carried out using IRAF <sup>3</sup> scripts which call DaophotII (Stetson 1994a). Reductions are usually finished within 6 hours of image acquisition. Team members have immediate network access to GMAN data, which were subsequently used for real-time scheduling during this event. Normalization is performed on-the-fly using a list of reference stars obtained from the MACHO data set. The reported DaophotII error bars for UTSO and WISE photometry have been increased by a factor of 2.0, to account for the typical scatter in a time series of constant stars from these images. The MJUO data used in this analysis were obtained manually from the raw frames after the event, using DaophotII operating within the IRAF environment; the uncertainties were estimated by

---

<sup>2</sup>Operated by the Association of Universities for Research in Astronomy, NOAO, under cooperative agreement with the National Science Foundation

<sup>3</sup>IRAF is distributed by the National Optical Astronomy Observatories, which is operated by the Association of Universities for Research in Astronomy, Inc., under contract to the National Science Foundation.

examining the variations of standard star ratios within and between frames. Data from CTIO were re-reduced using Allframe (Stetson 1994b).

The system and data collection of the MACHO experiment are described in Alcock et al. (1996c). The data are obtained simultaneously in two specially designed wide-pass filters with effective wavelengths of approximately 5150 Å and 6900 Å. Transformations from the MACHO instrumental photometry system to the standard  $V$  and  $R_{KC}$  system have been derived by comparisons with several thousand tertiary standard stars calibrated in the LMC. Checks of our photometry with published photometry in Baade’s Window confirm a zero point uncertainty of less than 0.1 mag in  $V$  and  $R$ , where this uncertainty is a conservative estimate of small zero point differences between fields monitored by MACHO in the bulge.

#### 4. Photometry of MACHO Alert 95–30

The source star in Alert 95–30 is located at  $\alpha = 18:07:04.26$ ,  $\delta = -27:22:06$  (J2000). The MACHO project’s identifier for this star is 101.21821.128. Alert 95–30 was detected by the MACHO Alert system at  $A \sim 1.8$  on Jul 24, 1995, approximately 22 days before the observed peak.

The location of the source star in an optical color–magnitude diagram (CMD),  $V = 16.21$  and  $(V - R) = 1.39$ , indicates this star passes the “clump giant” cuts defined in Alcock et al. (1996b). Figure 1 shows a single epoch CMD for a  $2 \times 2$  arcmin field surrounding the source star, which is indicated with a circle. We may be reasonably sure then that this star is located in the Galactic bulge and has a large radius. Microlensing fits to the rising portion of the light–curve predicted a high–magnification event for the giant source, which presented the possibility of source star resolution.

Subsequent observations indicated deviations from the standard microlensing model at  $A \sim 20$ , approximately 2 days before the projected peak. At this time, we mounted an aggressive program of photometry and spectroscopy to study these deviations thoroughly. Follow–up observations continued nightly past the observed peak until the star returned to its baseline state. Intermittent observations followed to determine accurately the baseline flux as measured at each site.

Figure 2 displays the MACHO 1995 bulge season light–curve of Alert 95–30 <sup>4</sup>. The alert date is indicated with an arrow, after which time the light–curve becomes heavily sampled with follow–up data. Data from all follow–up observatories have been included after determining the baseline flux in each passband. No microlensing fits are included in the figure, but it is

---

<sup>4</sup>We report an uncatalogued CCD trap which allowed several contaminated MACHO–red observations to pass through our processing stream. The majority of these were removed from the data set based upon their proximity to the bad columns and psf FWHM.

apparent that the data conform to the symmetric and achromatic shape expected of gravitational microlensing events, at least for magnification  $A \leq 20$ .

This conclusion is confirmed after fitting a normal microlensing curve to the combined dataset. Event parameters for this fit (fit 1 hereinafter) are listed in Table 2, and  $\chi^2$  statistics for each passband are listed in Table 3. However, near the peak of the event the data deviate from the expected light-curve (see Fig 3). This type of deviation is not unexpected in a high magnification microlensing event. We note that the standard point-source microlensing model allows infinite magnification when the source and lens are aligned. When the extended size of the source is considered, the magnification is limited, as the entirety of the source disk cannot be perfectly aligned with the lens. If we include an extra parameter in the fit to account for the angular size of a constant surface brightness source star (fit 2), we reduce  $\chi^2$  by 1084. The deviations near the peak of MACHO 95–30 are significantly reduced with this model, which we interpret as clear justification for the extended source microlensing interpretation.

The data in Table 3 indicate an extended source fit  $\chi^2$  per degree of freedom of approximately 1 for the GMAN follow-up data. The implication here is that the data scatter around the fit is what one would statistically expect due to measurement error. Thus, the data are in excellent agreement with the extended source microlensing fit, considering our photometry is at the 1 – 2% level, as indicated in column 3 of Table 3. However, the MACHO data exhibit  $\chi^2_{dof}$  between 3 – 4, which formally indicates a poor fit to the data. While it is obvious that this is indeed a gravitational microlensing event, such a poor fit might cast doubt on the extended source interpretation. Fits to data of magnification  $A < 10$ , which should be negligibly affected by extended source effects, display the same excessive scatter around the fit. We therefore conclude that the majority of this scatter is contained in baseline measurements, and should not adversely affect our interpretation of the data.

Figure 2 also presents a scaled schematic of this microlensing event using event parameters derived from fits with a limb-darkened source star (fit 3). Included are the lens’s Einstein radius expressed as  $\hat{t}/2$ , the source radius scaled to  $0.0756 R_E$ , and the trajectory of the lens across the extended face of the source star.

Figure 3 provides a visual comparison between the best standard microlensing fit to the data (dashed line) and microlensing of a limb-darkened extended source (solid line). Each passband was fit independently with a baseline parameter, while event parameters were derived from joint fits on the combined dataset. All fits were performed in the MINUIT environment (James 1994).

## 5. Determination of Stellar Parameters

Analysis of the stellar parameters of the source star in MACHO 95–30 (hereinafter referred to as the source star) is required if we are to use the additional information provided by  $u_*$  to characterize the lensing object. The most important parameters are its distance ( $L$ ) and radius

( $R_*$ ). Also valuable are estimates of the source temperature and surface gravity, which will help define the limb-darkening coefficients.

Figure 1 shows the fiducial line for the red giant branch of the metal-rich globular cluster NGC 6553 from Ortolani et al. (1990), plotted over the optical CMD for a  $2 \times 2$  arcmin field surrounding the source star. We note that the horizontal branch (HB) in this field is inclined like that of NGC 6553, due to the effect of differential reddening. Even though the morphology of the red giant branch of this cluster is similar to that of the MACHO field surrounding the microlensing event, the magnitude of the source star is fainter than expected, after we account for the different reddenings and distances to these sources (we adopt a bulge distance of 8 kpc). The smaller apparent luminosity could be due to differences in age, metallicity, or distance. From this diagram, we tentatively conclude that this star is either more metal-rich, or more distant than 8 kpc (or both) than the giants of similar color in NGC 6553.

### 5.1. Reddening

The reddening is patchy in the MACHO field where the source star is located. Figure 4 shows the amplitude vs. color of all the RR Lyr that we found in this field. The reddening vector is horizontal in this figure, so the color spread is mostly due to differential reddening within the field, as the RRab sequence in such a diagram should be very tight (Bono et al. 1997). There appear to be two zones of different obscuration, with  $E(B - V)$  ranging from 0.3 to 0.8 mag. The source star appears to be located in the region with smaller reddening, as measured from the colors of the three closest RR Lyr. We identified a total of two bulge RR Lyr type ab, and one RR Lyr type c, within 2 arcmin of the source star. The locations of these 3 RR Lyr are shown in the optical CMD (Figure 1) as triangles. The mean color of the two RRab is  $V - R = 0.54$ , and the mean color of the RRc is  $V - R = 0.46$ . From these colors we deduce  $E(V - R) = 0.34 \pm 0.05$ . Using the extinction law of Rieke & Lebofski (1985), we obtain  $A_V = 1.36$ ,  $E(B - V) = 0.44$ ,  $A_K = 0.15$ ,  $E(V - K) = 1.21$ ,  $E(J - H) = 0.15$ ,  $E(H - K) = 0.08$ , and  $E(J - K) = 0.23$ . The observed and dereddened photometric measurements of the source star are listed in Table 4.

### 5.2. Infrared Photometry

We observed the field of the source star with the CIRIM camera on the CTIO 1.5m telescope. The f/13.5 configuration yields a pixel scale of  $0.65 \text{ arcsec pixel}^{-1}$ . The detector is a  $256 \times 256$  HgCdTe NICMOS 3 array. Conditions on the night of September 24, 1996 were photometric. We used the  $J$ ,  $H$ , and  $K_s$  filters, and a five-position on-source dithering pattern optimally to expose the target field and collect the necessary frames for sky flats. Six 10-second coadds were obtained at each position in the dithering pattern for total exposures of 300 seconds in each filter. The individual IR images were reduced following standard procedure using dark and sky frames,

then shifted and combined to create the final images, which cover about 2 arcmin on a side. The photometric calibration was obtained by observing the UKIRT Faint Standard Star no. 1 (G158–100) just prior to observing the field of the source star. The standard star and program field were observed at identical airmasses ( $X = 1.2$ ), thus no extinction corrections were necessary. We find  $K = 9.98$ ,  $(J - K) = 1.12$ , and  $(H - K) = 0.26$  mag for the source star. We estimate an uncertainty of 0.05 mag in  $J$ ,  $H$ , and  $K$  from the photon statistics and aperture corrections. Figure 5 shows the optical–IR color–color diagram of stars one magnitude brighter than the horizontal branch in the  $2 \times 2$  arcmin field surrounding the source star, along with the sequences corresponding to field giants, field dwarfs, and Baade’s Window giants from Frogel & Whitford (1987). The colors of the source star are similar to Baade’s Window M giants, and we conclude that it is unlikely to be a field dwarf.

Figure 6 shows an expanded version of the reddening corrected  $K_0$  vs  $(V - K)_0$  optical–IR CMD for the bright stars found in this field. Overplotted are the fiducial lines corresponding to the red giant branches of the metal–rich globular clusters 47 Tuc from Frogel et al. (1981) and the metal–rich globular cluster NGC 6553 from Guarnieri et al. (1996), assuming a distance of 8 kpc for both populations. Figure 6 shows again that the source star is relatively faint with respect to the giants in these clusters. This suggests that the star is either more metal–rich than  $[Fe/H] = -0.4$ , and/or more distant than 8 kpc. As an additional comparison, we have plotted data from Frogel & Whitford (1987) for spectral type M3–5 giants from Baade’s Window (assuming a distance of 8 kpc), and our own estimated fiducial line for these stars. If we assume a solar composition for the source star ( $[Fe/H] = 0$ ), we obtain a distance of about  $D = 10$  kpc. The uncertainty in this distance is large; it assumes that all of the scatter about the fiducial line of BW giants is due to the line–of–sight depth of the bulge. It is possible that the source star is on the metal–rich tail of the distribution of bulge giant metallicities. Comparing the two globular cluster tracks in Figure 6 gives one a sense of the dependence of the red giant branch fiducial lines on metallicity. If the location of the source star in the CMD were entirely due to metallicity, it would be an extremely metal–rich star, which is less probable than a combination of distance and metallicity effects at work. Given the position of the source star in the CMD at the outer envelope of giants observed in Baade’s Window, we conclude that the source star is likely located on the “far” side of the bulge. Note that we would expect a giant star in the Sagittarius dwarf galaxy to be about 2 magnitudes fainter than the observed  $K_0$  magnitude of the source star (see also Section 5.3.3 below).

### 5.3. Spectroscopy

We have obtained spectra of the source star in several different observing runs, as will be discussed in Section 7. Here we analyze the spectra taken at the 4m Blanco telescope at CTIO with the R–C spectrograph and the Loral  $3K_1$  detector during the nights of 14 and 15 August, and 27 September, 1995. The first two spectra were taken 0.5 days before and after, respectively,

the peak of the microlensing event, while the lens was still in transit across the source face. The wavelength coverage of these spectra is from  $\lambda 6230$  to  $\lambda 9340$  Å. A HeNeAr comparison lamp was used, which provided the wavelength calibration. The exposures were 60 seconds long, and were taken at an airmass of 1.7. All the spectra were reduced in the standard way. The dispersion was  $1\text{Å pixel}^{-1}$ , and the resolution was  $5\text{Å}$ , as measured from the FWHM of the lines.

The additional spectrum from 27 September, 1995 was taken at an airmass of 1.1, with a total exposure time of 500 seconds. No independent wavelength calibration was obtained for this spectrum. The dispersion was  $2\text{Å pixel}^{-1}$ , and the resolution was  $8\text{Å}$ . The wavelength coverage of this spectrum, shown in Figure 7, was from  $\lambda 3890$  to  $\lambda 9830$  Å. This spectrum, taken 42.3 days after peak magnification, is very similar to the near-peak spectra. This further supports the microlensing interpretation, where the overall colors or spectral type must not change.

### 5.3.1. Spectral Typing

We determined the spectral type of the source star by direct comparison with the digital spectral atlas of late-type stars of Turnshek et al. (1985) and Kirkpatrick et al. (1991). This comparison was done visually after rebinning our CTIO spectra to lower resolution, and paying close attention to the match of the prominent TiO bands. There is a very close match of the spectra shown in Figure 7 with a spectral type M4 III, and we adopt this classification for the source star. The uncertainty in this classification is estimated to be one spectral subtype.

Using the spectral type we can check our estimate of the reddening of the source star by adopting the unreddened optical and infrared colors of the same type bulge giants. For an M4 III bulge star, Frogel & Whitford (1987) give  $(J - K)_0 = 0.90$  and  $(H - K)_0 = 0.18$ . and from the observed infrared colors we compute  $E(J - K) = 0.22$ , and  $E(H - K) = 0.08$ , respectively. These reddening values are in excellent agreement with the reddening derived from the optical photometry of the RR Lyr in this field (see Table 4).

### 5.3.2. CaII Triplet

The CTIO spectra allows us to determine independently the surface gravity ( $g$ ) of the source star. The spectral region covered includes the CaII triplet, which is strong and very sensitive to  $\log g$ . Other spectral lines in the region from  $\lambda 6400$  Å to  $\lambda 9200$  Å can be used for this purpose in M-type stars, like the NaI doublet at  $\lambda\lambda 8183, 8195\text{Å}$  (Kirkpatrick et al. 1991). However, the lines of the CaII triplet are the most suitable ones, because they have been studied and calibrated by a number of authors (Jones et al. 1984; Humphreys & Graham 1986; Diaz et al. 1989; Alloin & Bica 1989; Jorgensen et al. 1992; Erdelyi-Mendez & Barbuy 1991).

We measured the equivalent width of the CaII lines at  $\lambda 8498.06$  Å,  $\lambda 8542.14$  Å, and  $\lambda 8662.17$

Å in the three spectra obtained with two different resolutions, obtaining  $EW = 11.0 \pm 0.5$  Å, where the uncertainty is dominated by the location of the continuum. We used the local continuum bands at  $\lambda 8480$  Å,  $\lambda 8635$  Å, and  $\lambda 8905$  Å, defined by Jones et al. (1984), Diaz et al. (1989), and Alloin & Bica (1989), in order to make a direct comparison with their measurements and models. Note that the resolution of our spectra is similar to these other works.

We have also compiled published data (spectral type,  $T_{\text{eff}}$ ,  $\log g$ , and CaII– $EW$ ) on M–type stars, covering a wide range of temperatures and gravities. In some cases only the two strongest lines of the CaII triplet are measured, and we have scaled these accordingly in order to include the weaker line. Figure 8 shows the equivalent width vs M spectral subtype for dwarfs (V), giants (III), and supergiants (I). The position of the source star is shown with the box. This figure confirms the conclusions drawn from the IR photometry and spectral classification – the source is a giant star.

Figure 9 shows equivalent width vs  $\log g$ . The dotted lines show the  $\pm 1\sigma$  measurements for the source star. From this figure we conclude that  $\log g = 1.0 \pm 0.2$ . A similar value is obtained by applying the empirical relations found by Alloin & Bica (1989) and Diaz et al. (1989), and by slightly extrapolating the models of Jorgensen et al. (1992) and Erdelyi-Mendez & Barbuy (1991).

### 5.3.3. Radial Velocity

We have also measured the radial velocity of the source star. Unfortunately, we did not measure radial velocity standards, and have to rely on a wavelength calibration based on the HeNeAr lamps. From the two CTIO spectra of the August run we obtain  $V_r = -80 \pm 5$  km s<sup>-1</sup>. Even though the spectra from the August run have high enough resolution to measure velocities good to  $< 10$  km s<sup>-1</sup>, we consider that the most important source of uncertainty is the zero point.

We consider the possibility that the source star may be located in the Sgr dwarf galaxy. The Sgr dwarf galaxy discovered by Ibata et al. (1995) is much more extended than previously thought. RR Lyr belonging to this galaxy have been identified in fields close to the Galactic plane (Alard et al. 1996; Alcock et al. 1997). In fact, the Sgr galaxy extends as far as the field containing the source star, as shown by the one Sgr RR Lyrae type ab discovered in this field by Alcock et al. (1997). However, the radial velocity measured here rules out membership to the Sgr dwarf galaxy, which has  $V_r = +150$  km s<sup>-1</sup>.

The radial velocities of bulge giants in off-axis bulge fields have been measured by Minniti (1996) and Minniti et al. (1996). At the position of the MACHO field, the mean heliocentric radial velocity of bulge stars is estimated to be about 25 km s<sup>-1</sup>, with a velocity dispersion  $\sigma = 80$  km s<sup>-1</sup>. The radial velocity of the source star is, therefore, consistent with the velocities of bulge giants, supporting our assumption that this star belongs to the bulge population.

### 5.4. Stellar Parameters

We will derive the stellar parameters  $M$ ,  $T_{\text{eff}}$ ,  $L$ , and  $R$  for the source star in a variety of ways and compare the different values to estimate our uncertainties. When needed, we assume the solar values:  $T_{\odot} = 5730K$ ,  $\log g_{\odot} = 4.44$ , and  $M_{\text{bol}\odot} = 4.72$  mag. The following equations relate various stellar parameters:

$$\begin{aligned} (L/L_{\odot}) &= (R/R_{\odot})^2(T_{\text{eff}}/T_{\odot})^4 \\ (g/g_{\odot}) &= (M/M_{\odot})(R/R_{\odot})^{-2} \end{aligned}$$

We begin with the most simple method, adopting the typical stellar parameters of an M4 giant in the galactic bulge. We would expect the mass of the source star to be  $\sim 1M_{\odot}$ , the mass appropriate for a bulge giant according to the estimated age of the bulge (e.g. Holtzman et al. 1993). Using only the spectral type information (M4 III), we obtain  $T_{\text{eff}} = 3430$ ,  $M_{\text{bol}} = -2.7$  from Lang (1992), which gives  $R = 85R_{\odot}$ . Also, for an M4 III star,  $R = 83R_{\odot}$ , and  $T_{\text{eff}} = 3600$  from the recent calibrations of Dyck et al. (1996). These values are averages over several spectral sub-types. The dependence of radius on spectral type is such that for an M3 III star  $R \approx 60R_{\odot}$ , and for an M5 III star  $R \approx 100R_{\odot}$ .

The IR colors allow us to measure the effective temperature. For  $J - K_0 = 0.89$ ,  $T_{\text{eff}} = 3900 \pm 270$  from the calibration of Feast (1996). For  $V - K_0 = 5.03$ ,  $T_{\text{eff}} = 3600$  from the recent calibration of Bessell et al. (1997). The optical photometry also allows us to estimate the temperature of the source star. For  $(V - R)_0 = 0.93$ , we find  $T_{\text{eff}} = 3800 \pm 200$  by differential comparison with the giant star III-17 member of the globular cluster NGC 6553 analyzed by Barbuy et al. (1992). Comparing these values of temperature with those derived from the spectral type information, we adopt a temperature of  $T_{\text{eff}} = 3700 \pm 250$  for the source star, or  $\log(T/T_{\odot}) = -0.19 \pm 0.03$ .

Numerous bolometric corrections exist in the literature. We find  $BC_K(J - K) = 2.6$  and  $BC_K(V - K) = 2.7$  from Frogel & Whitford (1987) and Bessell et al. (1997),  $BC_H(M \text{ giants}) = 2.6$  from Bessell & Wood (1984), and  $BC_V(M4III) = -2.2$  (Lang 1992). These give  $m_{\text{bol}} = 12.4$ , 12.5, 12.6, and 12.6, respectively. We adopt  $m_{\text{bol}} = 12.5 \pm 0.1$  for the source star.

In order to compute the absolute magnitudes, we must assume a distance to the star. Adopting a distance of 8 kpc, or  $m - M_0 = 14.52$ , we obtain the absolute magnitudes  $M_V = +0.34$ ,  $M_K = -4.69$ , and  $M_{\text{bol}} = -2.1$  mag. This gives  $\log(L/L_{\odot}) = 2.69 \pm 0.04$ . We can immediately derive the radius,  $\log(R/R_{\odot}) = 1.72 \pm 0.06$  or  $R = 53 \pm 8R_{\odot}$ . However, the uncertainty here is underestimated given the systematic uncertainty in the adopted distance. From our arguments in Section 5.2, we adopt the distance to the source star of  $9 \pm 1$  kpc, giving a distance modulus  $m - M_0 = 14.77 \pm 0.25$ . Re-calculating the radius at this distance and incorporating the added uncertainty, we find  $M_{\text{bol}} = -2.25 \pm 0.27$  and thus  $R = 61 \pm 12R_{\odot}$ .

Lastly, we derive the mass of the source star using the measured value of  $\log g$  (Section 5.3). We find  $\log(g/g_{\odot}) = -3.44 \pm 0.08$  and  $M \sim 0.8 - 2.5M_{\odot}$ . The mass derived in this manner is quite

uncertain. The largest mass values are unlikely given the age of the bulge  $t \approx 10$  Gyr (Holtzman et al. 1993). However, a mass slightly larger than  $1 M_{\odot}$  is consistent with the source star having a high metallicity.

To summarize, we adopt the following stellar parameters for the source star in MACHO Alert 95–30, which we categorize as an M4 bulge giant:

$$L = 600 \pm 200 L_{\odot},$$

$$T_{\text{eff}} = 3700 \pm 250 K,$$

$$\log g = 1.0 \pm 0.2,$$

$$R = 61 \pm 12 R_{\odot},$$

$$D = 9 \pm 1 \text{ kpc},$$

$$M \approx 1.0 M_{\odot},$$

$$[Fe/H] \approx 0.$$

## 6. Determination of Event Parameters

### 6.1. Effect of Limb–Darkening on the Photometry

We now integrate an approximate limb–darkening law into the microlensing model, to extract more realistic event parameters than those derived with a constant surface brightness disk. Limb–darkening coefficients for GMAN’s standard R and V passbands exist in the literature for  $T_{\text{eff}} = 3500$  K,  $\log g=1$  for the quadratic form of Equation 3 (Claret, Díaz-Cordovés, & Giménez 1995; Díaz-Cordovés, Claret, & Giménez 1995). Limb–darkening coefficients were also calculated for MACHO’s non–standard passbands (Claret 1996). These coefficients are listed in Table 5.

Including this brightness profile in the extended source model further improves the fit  $\chi^2$  by 9 (see Table 3, fit 3). While this improvement is formally significant, its interpretation here appears unclear. Comparison of fits 2 and 3 in Table 3 shows no clear trend between data sets, which effectively washes out any overall conclusions about the significance of the model. However, we do regard the limb–darkened parameters as the more realistic interpretation of the data. Comparison of optical and *infrared* photometry during a lens transit should detect significant color terms as a result of source limb–darkening (Gould & Welch 1996), which would then provide a more robust test of stellar atmosphere models.

## 6.2. Implications for Lens Mass

The limb-darkened fit to finite source microlensing provides a direct measurement of  $u_* \equiv \theta_*/\theta_E = 0.0756$ , i.e. the angular size of the star as a fraction of the Einstein ring angle. To convert this into physical units, we need an estimate of the angular radius  $\theta_*$  of the source star. The analysis in Section 5 indicates  $R_* = 61R_\odot$  and  $L = 9 \text{ kpc}$ , giving  $\theta_* = 31.5 \mu\text{arcsec}$  and thus  $\theta_E = 0.417 \text{ milliarcsec}$ . The Einstein diameter crossing time  $\hat{t}$  is measured similarly to the usual point-source case, so this provides the proper motion of the lens with respect to the source star  $\omega \equiv 2\theta_E/\hat{t} = 21.5 \text{ km s}^{-1} \text{ kpc}^{-1} = 4.51 \text{ mas/yr}$ .

Thus, an extended source microlensing event provides us with 2 constraints  $\hat{t}$  and  $\omega$  on the 3 unknowns  $M$ ,  $x$  and  $v_\perp$  of the lens. In the following, it is convenient to define  $\hat{v} \equiv \omega L = v_\perp/x$  to be the relative velocity of the lens projected back to the source plane (cf Han & Gould 1996); substituting  $r_E = \hat{v}x\hat{t}/2$  into Eq. 2, we obtain a one-to-one relationship between the lens mass and distance,

$$M(x) = \frac{\hat{v}^2 \hat{t}^2 c^2}{16 GL} \frac{x}{1-x}. \quad (4)$$

(By symmetry, this is the same as Eq. 6 of Alcock et al. (1995b) exchanging observer and source, i.e. with  $\hat{v}$  instead of  $\tilde{v}$ , and  $x \leftrightarrow 1-x$ .) For the observed values of  $\hat{v} = 193 \text{ km s}^{-1}$ ,  $\hat{t} = 67.3$  days, we have  $M(x) = 0.192 M_\odot x/(1-x)$ , thus the lens may be either a low-mass star roughly half-way to the source, or a more massive star closer to the source. Figure 10 shows  $M(x)$  for the event parameters given in Table 3 (fit 3), and the radius and distance of the source star obtained in Section 5. Since our proper motion error is dominated by uncertainty in the source radius, we also include  $M(x)$  contours for  $R_* = 61 \pm 12R_\odot$ .

We may obtain additional constraints on  $x$  by using a model for the distributions of sources and lenses, since the likelihood of obtaining the observed value of  $\hat{v}$  is also a function of  $x$ .

For given lens mass, the rate of microlensing is proportional to

$$d\Gamma \propto \sqrt{x(1-x)} \rho_L(x) v_\perp f_S(\mathbf{v}_S) f_L(\mathbf{v}_L) dx d\mathbf{v}_S d\mathbf{v}_L. \quad (5)$$

where  $\rho_L$  is the density of lenses at distance  $x$ ,  $f_L(\mathbf{v}_L)$  and  $f_S(\mathbf{v}_S)$  are the lens and source velocity distribution functions (normalized to unity) in the plane perpendicular to the line of sight. The source and lens velocities  $\mathbf{v}_S, \mathbf{v}_L$  are related to  $\hat{\mathbf{v}}$  by  $\mathbf{v}_L = (1-x)\mathbf{v}_\odot + x(\mathbf{v}_S + \hat{\mathbf{v}})$ , where  $\hat{\mathbf{v}} = (\hat{v} \cos \phi, \hat{v} \sin \phi)$  and  $\phi$  is the (unknown) direction of the relative proper motion.

Given a model for  $\rho_L, f_S, f_L$ , we may integrate Eq. 5 and thus obtain joint probability distributions for any of the variables. Since we have measured  $\hat{v}$ , and the lens mass depends on only one unknown ( $x$ ), we need to consider the joint probability distribution of events in the  $(x, \hat{v})$  plane, and then marginalize to get a probability distribution of  $x$  given the observed value of  $\hat{v}$ .

Thus, we change variables from  $d\mathbf{v}_L$  to  $d\hat{v} d\phi$ , giving

$$d\Gamma \propto \sqrt{x(1-x)} \rho_L(x) v_\perp f_S(\mathbf{v}_S) f_L(\mathbf{v}_L) dx d\mathbf{v}_S \left| \frac{\partial \mathbf{v}_L}{\partial (\hat{v}, \phi)} \right| d\hat{v} d\phi. \quad (6)$$

We then substitute for  $\mathbf{v}_L$  and  $v_\perp$  and integrate over the unknowns  $\mathbf{v}_S$  and  $\phi$ , giving a likelihood as a function of distance for given  $\hat{v}$ ,

$$\mathcal{L}(x; \hat{v}) = \left. \frac{d\Gamma}{dx d\hat{v}} \right|_{\hat{v}} \propto \sqrt{x(1-x)} \rho_L(x) \hat{v}^2 x^3 \int \int f_S(\mathbf{v}_S) f_L((1-x)\mathbf{v}_\odot + x(\mathbf{v}_S + \hat{\mathbf{v}})) d\mathbf{v}_S d\phi, \quad (7)$$

This result may be understood as follows: the integrals are over all combinations of source and lens velocity which give rise to the observed  $\hat{v}$ . The  $\sqrt{x(1-x)}$  and  $\rho_L$  terms arise from the  $x$ -dependence of the Einstein radius and density of lenses, respectively. There is a factor of  $v_\perp = \hat{v}x$  because a given lens contributes a lensing rate  $\propto v_\perp$ , and a factor of  $x^2\hat{v}$  from the Jacobian  $\det(\partial\mathbf{v}_L/\partial(\hat{v}, \phi))$ .

To evaluate Eq. 7, we adopt a disk velocity dispersion of  $30 \text{ km s}^{-1}$  in each direction, with a flat rotation curve of  $220 \text{ km s}^{-1}$ . We adopt a bulge velocity dispersion of  $80 \text{ km s}^{-1}$  in each direction, and no bulge rotation. For the density profiles, we use a standard double-exponential disk, and a barred bulge as in Han & Gould (1995). The source is located at galactic coordinates  $l = 3.73^\circ$ ,  $b = -3.30^\circ$ , and we assume  $L = 9 \text{ kpc}$ ,  $R_0 = 8 \text{ kpc}$ , so the source is behind the galactic center. We assume the source is a member of the bulge, so we take  $f_S$  to be the above velocity distribution function of bulge stars, and then we evaluate Eq. 7 separately for  $\rho_L, f_L$  appropriate for lenses either in the disk or the bulge.

Figure 10 shows the result of Equation 7 as a function of lens distance, for the observed  $\hat{v} = 193 \text{ km s}^{-1}$ . The lower solid line shows disk lenses only, and the upper solid line shows the sum of disk + bulge lenses; the relative areas indicate that there is about an 80% probability that this lens belongs to the bulge.

We define a median distance  $x_{\text{med}}$  such that half of the integrated likelihood arises from  $x < x_{\text{med}}$ , giving  $x_{\text{med}} = 0.77$  and a median mass estimate of  $M_{\text{med}} = 0.67 M_\odot$ . Similarly, we define a 90% confidence interval  $(x_1, x_2)$  such that 5% of the integrated likelihood arises from each of  $x < x_1$  and  $x > x_2$ ; the resulting interval is  $0.52 < x < 0.943$ , which translates into a mass interval of  $0.21$  to  $3.2 M_\odot$ . These results are relatively insensitive to the details of the galactic model, since the constraints on  $x$  are dominated by the drop in  $\rho_{\text{Bulge}}$  for  $x \lesssim 0.6$  and by the geometrical factor  $\sqrt{x(1-x)}$  for  $x \rightarrow 1$ .

For reference, Figure 11 shows  $\hat{v} \int \mathcal{L}(x; \hat{v}) dx$ , i.e. the lensing rate per unit  $\log \hat{v}$  for disk and bulge lenses. The observed value of  $\hat{v} = 193 \text{ km s}^{-1}$  is well within the range of expected values. The areas under the two curves reflect the fact that bulge lenses produce about 3 times the event rate of disk lenses for the above models. This figure shows that there is a large overlap in the distributions; events with  $\hat{v} \lesssim 150 \text{ km s}^{-1}$  are produced almost entirely by bulge lenses, but the more common events with larger  $\hat{v}$  arise from both disk and bulge lenses; thus, proper motion measurements towards the bulge are not as useful as parallax measurements for constraining the lens distance. (This has been previously noted by Han & Gould (1995)).

Note that this is distinctly different from the LMC case, where either proper motion or

parallax measurements provide a good separation of the various lensing populations (Gould 1996).

### 6.3. Constraints on Lens Luminosity

As seen above, if the lens is more distant than  $x > 0.9$ , it has a relatively large mass. If it is a hydrogen-burning star, we can constrain this possibility as follows. For the above proper motion of  $\omega \approx 4.5$  mas/year, the lens is completely unresolved from the source during our observations, thus the observed light-curve of our ‘object’ is simply the sum of that from the source, the lens and possibly other superposed stars.

Any flux from the lens would add a constant un-magnified baseline which would distort the microlensing fit. Although in most cases this additional flux would be a small fraction of the flux of the source star, with the high precision measurements here this would be detectable even if the lens is considerably fainter than the source.

We have fit “blended” microlensing to data of magnification  $A < 10$ . This fit is of the form  $f_i(t) = A(t)f_{0i} + f_{Ui}$ , for  $i =$  each passband, where  $f_{0i}$  is the baseline flux of the source star and  $f_{Ui}$  is the total flux of unlensed stars superposed on the source, i.e. the sum of flux from the lens and any other superposed stars.

We note that the  $\chi^2_{dof}$  of all light-curves in these blended fits are similar to those in the extended source fits. We therefore exclude the MACHO data in our lens brightness estimate due to excessive baseline scatter; however, this turns out to be unimportant. The most follow-up data with  $A < 10$  are contained in the CTIO and UTSO observations. For the CTIO R, UTSO R, and UTSO V passbands, we find  $f_{Ui}/f_{0i} \approx (-0.021 \pm 0.016)$ ,  $(-0.019 \pm 0.017)$ , and  $(-0.015 \pm 0.016)$ , respectively, consistent with zero flux from the lens. For completeness, we note that similar results are obtained from the MACHO data, with  $f_{Ui}/f_{0i} \approx (-0.012 \pm 0.017)$  and  $(-0.026 \pm 0.018)$  for MACHO V and MACHO R, respectively. MJUO and Wise data did not contain enough baseline observations to determine accurately the amount of unlensed flux. In the following, we take  $0 \pm 0.02$  as a conservative limit.

If the lens is a main-sequence star, we may predict its apparent brightness using the mass-distance relation of Eq. 4. Assuming a main-sequence V-band mass-luminosity relation  $L/L_\odot = (M/M_\odot)^{3.5}$ , and 1.5 magnitudes of extinction, we find that the apparent brightness of a main-sequence lens would be e.g. 1% of that of the source star for  $x = 0.83$ , and 10% for  $x = 0.90$ . Note that the implied lens brightness *increases* with distance since the rapid rise in  $M(x)$  outweighs the  $r^{-2}$  term; note also that a giant lens is excluded at any distance.

Instead of applying a sharp limit  $x < 0.88$ , it is more rigorous to multiply the likelihood function of Eq. 7 by the Gaussian probability that the lens brightness is consistent with the above constraint on  $f_U/f_0$ . This causes a rapid roll-off in the likelihood function for  $D_L > 7.5$  kpc, as shown by the dotted curves in Figure 10. Assuming a main-sequence lens, we can re-compute the

constraints on  $x$  and  $M$  from the likelihood function with the brightness factor, giving a median  $x = 0.73$ , a mass of  $M_{med} = 0.53 M_{\odot}$ , and 90% confidence intervals of  $0.48 < x < 0.84$  and  $0.18 < M < 1.05 M_{\odot}$ . Thus, the inclusion of the lens brightness constraint reduces the median mass only slightly, but considerably strengthens the upper limit.

## 7. Spectral Variation during MACHO 95–30

In addition to the CTIO observations discussed in Section 5.3, we have obtained spectra at Mount Stromlo and Keck<sup>5</sup> Observatories. Table 6 lists the complete catalogue of spectroscopic observations of this event. Figure 12 schematically shows the location of the lens with respect to the source when these different observations were made. Nightly spectra of the source star were taken between August 18 and 25, 1995 (from 2.8 to 9.8 days after peak magnification), with the Cassegrain spectrograph at the MSO 74-inch telescope. They cover the wavelength interval 6240–6770 Å, with a dispersion of 0.90 Å per pixel, and a resolution FWHM = 4.6 Å as determined from the comparison lamp spectra. The total exposures were typically 1000 seconds long. These MSO spectra are wavelength calibrated and sky subtracted, but not fluxed. The S/N per resolution element is listed in Table 6, along with other relevant data.

The CTIO and MSO spectra have similar resolution, with the exception of the September 27 CTIO spectrum, which has lower resolution. We rebinned the CTIO and MSO spectra in order to compare them directly. Figure 13 shows the spectral sequence, which constitutes one of the most extensive and homogeneous series of spectroscopic observations of a microlensing event to date (see also Benetti et al. 1995). It is clear that the microlensing does not change the spectral type of the star, nor does it strongly affect the major spectral features. However, subtle effects may appear in some spectral lines, as discussed by Loeb & Sasselov (1995), which warrants a more careful comparison among the spectra.

Before this discussion, we note that the MSO spectrum of August 18 (the first spectra taken *after* the lens transit) is anomalous, showing a dip at  $\lambda 6520\text{Å}$  that looks like an unidentified bandhead. Although we have examined several possible sources for this feature, including checking the flat fields and comparing the spectra of other stars in the field, the cause of this dip is still unexplained.

Each spectrum was divided by the median combination of all spectra (this operation was repeated before and after continuum subtraction, in order to account for possible differences due to flux calibration of the CTIO spectra but not of the MSO ones). Figure 14 shows the sequence of these ratios. While there are no strong deviations, the two spectra taken closest to maximum magnification show stronger H $\alpha$  than the rest. Also, these two spectra show stronger TiO bands than the following ones. The total TiO absorption, however, started to climb steadily after 18

---

<sup>5</sup>The Keck telescope project was made possible by a generous grant from the W.M. Keck Foundation.

August, 1995. We measured the equivalent widths of several spectral features of interest within 6240–6770 Å with the SPLIT package within IRAF. Figure 15 shows the equivalent width of H $\alpha$ , and the combined intensity of 4 TiO bands in the 6650–6750 Å region. Included are conservative error bars based upon uncertainty in placing the local continuum. The equivalent width of the H $\alpha$  line was scaled to the equivalent width measured in the HIRES spectra of 18 and 19 August, 1995. These equivalent widths were measured with respect to the local pseudo continuum, in the same way for all the spectra, in order to avoid systematic effects.

While we cannot explain in detail the behavior of these spectral features, changes in the equivalent width of these lines have been predicted by Loeb & Sasselov (1995). These changes are due to limb brightening effects in the cores of resonance lines (like H $\alpha$ ) due to a very extended photosphere. Resonant line scattering may also affect the optical TiO bands in the case of M giants like the MACHO 95–30 source (Sasselov 1997). Detailed modeling of the spectra of this event in particular is needed, as this will help with the interpretation of forthcoming similar events.

Three spectra were also taken in the nights of August 18, August 19, and August 21, about 5 hours later than the MSO spectra, using HIRES at the Keck 10-m telescope. These high resolution spectra also have high S/N, as listed in Table 6, which includes the S/N per resolution element of the lowest and highest orders. The spectra of August 18, August 19, and August 21 consist of 30, 25, and 40 orders, respectively. The blue region below about 4000Å covered in the August 21 spectrum does not have much information due to low counts. We have checked different resonance lines (CaII, H $\alpha$ , H $\beta$ , H $\gamma$ , etc), finding no large variations. The August 21 spectrum has coverage extending to the blue, including the Ca H and K lines, but misses the H $\alpha$  line. The spectra of August 18 and 19 do not include these Ca lines. The H $\alpha$  equivalent width differs by only 4% between August 18 and 19, as measured from the high quality HIRES spectra (1.087 vs 1.039Å). This variation occurs in the core of the line. Otherwise, there is no significant change between the H $\alpha$  profiles of August 18 and 19. The strong TiO band heads at  $\lambda\lambda$  4954, 5166, and 5447 Å are present in all three HIRES spectra. The difference of about 10% in strength of these bands between August 18 and 21 seen in the MSO spectra is confirmed.

We have also fit the NaI (D) line profiles in the HIRES spectra with an interstellar cloud model which uses 12 clouds over the velocity range  $-60.8 \text{ km s}^{-1}$  to  $+202.3 \text{ km s}^{-1}$ . The clouds with extreme velocities only fit one line of the Na doublet because of problems with the continuum determination and blending with other lines. The interstellar clouds indicate that the star is at a great distance and therefore it is certainly a giant, as discussed in Section 5.3.

We also measured the radial velocities of the MSO spectra using the cross-correlation routine FXCOR within IRAF. From the MSO spectra, we measure a mean velocity of  $V_r = -76 \pm 4 \text{ km s}^{-1}$ , which is in excellent agreement with the mean velocity of  $V_r = -80 \pm 5 \text{ km s}^{-1}$  from the CTIO spectra, reduced and calibrated independently (Section 5.3). The velocities of the eight MSO spectra agree with each other within an rms of  $12 \text{ km s}^{-1}$ . We measured also the radial velocity of the August 21 HIRES spectrum,  $V_r = -86.2 \pm 3.9 \text{ km s}^{-1}$ , using the strong Cr lines at  $\lambda\lambda$  4254,

4274, and 4289 Å. All these velocities are in excellent agreement, and we adopt a final value of  $V_r = -81 \pm 5 \text{ km s}^{-1}$  for the source star in MACHO 95–30.

Subtle radial velocity variations (of the order of  $1 - 2 \text{ km s}^{-1}$ ) may also be expected during microlensing events such as this one (Maoz & Gould 1994), and can give an independent measurement of the proper motion. Alternatively, combining the radial velocity variation with the extended source magnification effect, one can determine the projected rotation velocity of the star (Gould 1997). We note that detecting such velocity differences may be possible using the HIRES spectra, after detailed corrections and modeling that are beyond the scope of the present paper.

In summary, we have obtained a large number of spectra of the microlensed source star during MACHO Alert 95–30. These spectra show subtle variations, which support the predictions of existing microlensing and stellar models. These spectra demonstrate that differential magnification of an extended source star during a gravitational microlensing event may be used to probe otherwise inaccessible stellar atmosphere “fine structure”.

## 8. Conclusions

We have observed the breakdown of the point–source approximation for the first time in a “normal”, single lens microlensing event. This deviation was anticipated based upon real–time information provided by MACHO–GMAN, and dynamically scheduled for GMAN follow–up observations throughout the event. In effect, we have “resolved” a star which is  $\sim 9 \text{ kpc}$  from Earth. The resulting deviation from point–source microlensing provides a second constraint equation for the system, partially reducing the ambiguity between lens mass, position, and transverse velocity.

Measurement of the effective radius of the source star during the microlensing event provides an estimate of the scale of the lens’s Einstein radius. With additional information about the radius and distance of the source, we determine the angular velocity of the lens with respect to our line of sight to the source. This allows a statistical estimate of the lens mass by assuming velocity distributions of sources and lenses. We conclude that this event is due to lensing by an object of mass  $0.67_{-0.46}^{+2.53} M_{\odot}$  (at the 90 % confidence level), such as a white dwarf or a neutron star, which is most likely in the bulge (80 % c.l.). If the lens is a main–sequence star, the upper end of this mass range is excluded, and our mass estimate becomes  $0.53_{-0.35}^{+0.52} M_{\odot}$ . The results of this paper are attributable to the coordinated efforts of GMAN observers, and are a robust endorsement for microlensing follow–up implemented at 1–m class telescopes.

We have also detected for the first time subtle variations in the spectra of a star undergoing microlensing. Anomalously strong equivalent widths of  $\text{H}\alpha$  and  $\text{TiO}$  were detected while the lens was in transit across the source, an effect anticipated due to varying line widths across the face of the star. Given our ability to predict limb crossings in real–time, this technique may be used to map out the center–to–limb variations in the spectrum of a future microlensed source.

### Acknowledgments

We would like to thank Antonio Claret for providing limb-darkening coefficients for the MACHO passbands. The authors also wish to thank the skilled GMAN observers at UTSO, Boyd Duffee and Felipe McAuliffe. We are very grateful for the skilled support of the staff and observers at CTIO, in particular Bob Schommer, for flexibility in scheduling GMAN follow-up observations. We thank the NOAO for making nightly use of the CTIO 0.9 m telescope possible.

Astronomy at Wise Observatory is supported by grants from the Israel Science Foundation.

The MOA group thanks the Directors of MJUO and KEK for support, and Messrs G. Nankivell and N. Rumsey and staff members of Perth Observatory, MJUO, Camex Ltd and the Auckland University Science Faculty Workshop for assistance. Grants by Auckland and Victoria Universities, NZ/Japan Foundation, Ministry of Education, Science, Sports and Culture of Japan, KEK Laboratory, NZ Lottery Grants Board, NZ Ministry of Research, Science and Technology and the NZ Marsden Fund are gratefully acknowledged.

Work performed at LLNL is supported by the DOE under contract W7405-ENG-48. Work performed by the Center for Particle Astrophysics personnel is supported in part by the Office of Science and Technology Centers of NSF under cooperative agreement AST-8809616. Work performed at MSSSO is supported by the Bilateral Science and Technology Program of the Australian Department of Industry, Technology and Regional Development. WJS is supported by a PPARC Advanced Fellowship. KG acknowledges support from DOE Outstanding Junior Investigator, Alfred P. Sloan, and Cottrell awards. CWS thanks the Sloan, Packard and Seaver Foundations for their generous support.

## REFERENCES

- Abe, F., et al., 1997, in IAP Colloquium on “Variable Stars and the Astrophysical Returns of Microlensing Surveys”, ed. R. Ferlet, in press
- Alard, C. et al., 1995, ESO Messenger, 80, 31
- Alard, C., Mao, S. & Guibert, J., 1995, A&A, 300, L17
- Alard, C. et al., 1996, ApJ, 458, L17
- Albrow, M. et al., 1997, in IAP Colloquium on “Variable Stars and the Astrophysical Returns of Microlensing Surveys”, ed. R. Ferlet, in press
- Alcock, C. et al., 1995a, ApJ, 445, 133
- Alcock, C. et al., 1995b, ApJ, 454, L125
- Alcock, C. et al., 1996a, ApJ, 463, L67
- Alcock, C. et al., 1996b, ApJ, submitted (astro-ph/9512146)
- Alcock, C. et al., 1996c, ApJ, submitted (astro-ph/9606165)
- Alcock, C. et al., 1996d, IAU Circ., 6361
- Alcock, C. et al., 1997, ApJ, 474, 217
- Alloin, D. M., & Bica, E., 1989, A&A, 217, 57
- Aubourg, E. et al., 1995, A&A, 301, 1
- Barbu, B., Castro, S., Ortolani, S., & Bica, E., 1992, A&A, 259, 607
- Benetti, S., Pasquini, L., & West, R. M., 1995, A&A, 294, L37
- Bennett, D. P., & Rhie, S. H., 1996, ApJ, 472, 660
- Bessell, M. S., & Wood, P. R. 1984, PASP, 96, 247
- Bessell, M. S., Castelli, F., & Plez, B. 1997, preprint
- Binney, J. J., Gehrard, O. E., & Spergel, D., 1996, MNRAS, in press (astro-ph/9609066)
- Bono, G., Caputo, F., Castellani, V., & Marconi, M., 1997, A&A, in press
- Carney, B. W., Fulbright, J. P., Terndrup, D. M., Suntzeff, N. B., & Walker, A. R., 1995, AJ, 110, 1674
- Claret, A., Díaz-Cordovés, J., & Giménez, A., 1995, A&AS, 114, 247

- Claret, A., 1996, Private communication
- Crotts, A. P. S., 1996, astro-ph/9610067
- Diaz, A., Terlevich, E., & Terlevich, R., 1989, MNRAS, 239, 325
- Díaz-Cordovés, J., Claret, A., & Giménez, A., 1995, A&AS, 110, 329
- Di Stefano, R. & Esin, A. A., 1995, ApJ, 448, L1
- Dyck, H. M., Benson, J. A., van Belle, G. T., & Ridgway, S. T., 1996, AJ, 111, 1705
- Erdelyi-Mendez, M., & Barbuy, B., 1991, A&A, 241, 176
- Feast, M. W., 1996, MNRAS, 278, 11
- Frogel, J. A., & Whitford, A. E., 1987, ApJ, 320, 199
- Frogel, J. A., Persson, S. E., & Cohen, J. G., 1981, ApJ, 246, 842
- Gondolo, P., et al., 1996, astro-ph/9610010
- Gould, A., 1994, ApJ, 421, L71
- Gould, A., 1996, PASP, 108, 465
- Gould, A., 1997, ApJ, Submitted
- Gould, A. & Loeb, A., 1992, ApJ, 396, 104
- Gould, A. & Welch, D. L., 1996, ApJ, 464, 212
- Griest, K. et al., 1991, ApJ, 372, L79
- Guarnieri, D., et al., 1996, in “Science with the HST II”, eds. P. Benvenuti, D. Macchetto, & E. Schreier (STScI: Baltimore), p. 338
- Han, C. & Gould, A., 1995, ApJ, 447, 53
- Han, C. & Gould, A., 1996, ApJ, 467, 540
- Holtzman, J., et al., 1993, AJ, 106, 1826
- Humphreys, R. M., & Graham, J. A., 1986, AJ, 91, 522
- Ibata, R., Gilmore, G., & Irwin, M. J., 1995, Nature, 370, 194
- James, F., 1994, CERN Program Library Long Writeup D506.
- Jones, J. E., Alloin, D. M., & Jones, B. T., 1984, ApJ, 283, 457

- Jorgensen, U. G., Carlsson, M., & Johnson, H. R., 1992, *A&A*, 254, 258
- Kiraga, M., & Paczyński, B., 1994, *ApJ*, 430, L101
- Kirkpatrick, J. D., Henry, T. J., & McCarthy, D. W., 1991, *ApJS*, 77, 417
- Lang, K. R. 1992, *Astrophysical Data* (New York: Springer-Verlag)
- Loeb, A., & Sasselov, D., 1995, *ApJ*, 449, L33
- Mao, S. & Paczyński, B., 1991, *ApJ*, 374, L37
- Maoz, D., & Gould, A., 1994, *ApJ*, 425, L67
- Minniti, D., 1996, *ApJ*, 459, 579
- Minniti, D., Liebert, J. W., Olszewski, E. W., & White, S. D. M., 1996, *AJ*, 112, 590
- Nemiroff, R. J. & Wickramasinghe, W. A. D. T., 1994, *ApJ*, 424, L21
- Ortolani, S., Barbuy, B., & Bica, E., 1990, *A&A*, 236, 362
- Paczyński, B, 1991, *ApJ*, 371, L63
- Paczyński, B, 1996, *ARA&A*, In press
- Paczyński, B, et al., 1995, *BAAS*, 187, # 14.07
- Peng, E. W., 1997, *ApJ*, 475, 43
- Pratt, M.R. et al., 1995, In *Astrophysical Applications of Gravitational Lensing*, IAU Symp. 173, eds. Kochanek, C.S. & Hewitt, J.N, Kluwer. (astro-ph/9508039)
- Renault. C, et al., 1996, *A&A*, submitted (astro-ph/9612102)
- Rieke, G., & Lebofski, M., 1985, *ApJ*, 288, 618
- Sasselov, D., 1997, in IAP Colloquium on “Variable Stars and the Astrophysical Returns of Microlensing Surveys”, ed. R. Ferlet, in press
- Stetson, P. B., 1994a, *Daophot II User’s manual*.
- Stetson, P. B., 1994b, *PASP*, 106, 250
- Turnshek, D. E., Turnshek, D. A., Craine, E. R., & Boesjaar, P. C., 1985, *An Atlas of Digital Spectra of Cool Stars* (Tucson: Western Research Co.)
- Udalski, A., Szymański, M., Kaluźny, J., Kubiak, M., Krzemiński, W., Mateo, M., Preston, G. W., & Paczyński, B., 1994a, *Acta Astronomica*, 44, 165

Udalski, A., Szymański, M., Mao, S., Di Stefano, R., Kaluźny, J., Kubiak, M., Mateo, M. & Krzemiński, W., 1994b, *ApJ*, 436, L103

Witt, H. J., & Mao, S., 1994, *ApJ*, 430, 505

Zhao, H., Rich, R. M., & Spergel, D. N., 1996, *MNRAS*, 282, 175

Fig. 1.— Single epoch optical  $V$  vs  $V - R$  color-magnitude diagram of the field surrounding the source star, which is indicated with a filled circle. Three RR Lyr used to estimate the reddening are plotted as triangles. The fiducial loci of the giant branch of the metal-rich globular cluster NGC 6553 ( $[Fe/H] = -0.2$ ) from Ortolani et al. (1990) is also indicated.

Fig. 2.— 1995 light-curve of MACHO Object 101.21821.128 (Alert 95–30). The data represent MACHO-GMAN observations of this event in all passbands within a window of 70 days around peak magnification. The date this event was detected by the MACHO Alert system is indicated with an arrow. An additional schematic relates the scale of the lens’s Einstein radius to the angular size of the source star, and indicates transit of the lens across the source face.

Fig. 3.— Peak of MACHO Alert 95–30, showing the best standard microlensing fit to the data ( - - - ) and an extended source microlensing fit incorporating source limb-darkening (—).

Fig. 4.— Amplitude vs. color of the RR Lyr type ab in the MACHO field where the event is located. The two RRab closest to the source star are indicated with asterisks. We find  $A_V = 1.35$  mag.

Fig. 5.— Optical-infrared  $(V - K)_0$  vs  $(J - K)_0$  color-color diagram for the giants brighter than 1 mag above the horizontal branch in the field surrounding the source star. The fiducial loci of field giants, dwarfs, and Baade’s Window giants from Frogel & Whitford (1987) are indicated with the solid, short-dash, and long-dash lines, respectively.

Fig. 6.— Optical-IR  $K_0$  vs  $(V - K)_0$  color-magnitude diagram of the field surrounding the source star. The fiducial loci of the giant branches of the metal-rich globular clusters 47 Tuc ( $[Fe/H] = -0.7$ ), and NGC 6553 ( $[Fe/H] = -0.2$ ) from Guarnieri et al. (1996) are indicated. Additionally, we have plotted BW M3–5 giants (Frogel & Whitford, 1987) as small crosses and drawn our own estimated fiducial line through these points.

Fig. 7.— Baseline spectrum of the source star obtained at CTIO on September 27, 1995, 42 days after maximum magnification. The flux calibration is unreliable beyond  $9000\text{\AA}$ .

Fig. 8.— CaII equivalent width in  $\text{\AA}$  vs M spectral sub-type for dwarfs (circles), giants (asterisks), and supergiants (triangles). The box encloses the  $\pm 1\sigma$  measurements of the source star in MACHO 95–30.

Fig. 9.— CaII equivalent width in  $\text{\AA}$  vs  $\log g$ , with the dotted lines indicating the CaII equivalent width of the source star in MACHO 95–30 ( $\pm 1\sigma$ ).

Fig. 10.— Lens mass plotted as a function of its distance, using Equation 4. This assumes a  $61R_\odot$  source, with error contours provided at  $\pm 12R_\odot$ , and event parameters listed in Table 3 (fit 3). The solid likelihood curves show relative probabilities for disk and bulge lenses as a function of their distance. The dotted lines include an upper limit on the brightness of a main-sequence lens.

Fig. 11.— Lensing rates per unit  $\log \hat{v}$  for disk and bulge lenses, indicated with the solid and dashed lines, respectively.

Fig. 12.— Spectral observations listed in Table 6 plotted on the source plane. The relative sizes of the star (solid circle) and the lens’s Einstein radius (dotted circle) are plotted to scale, in units of  $R_E$ . The solid points show the position of the lens at the different times when spectra were taken. The observatories where the spectra were taken are indicated with the tick marks.

Fig. 13.— Spectra of the source star taken at CTIO and MSO. All of these have similar resolution, except for the top one. Note  $H\alpha$  at  $\lambda 6553 \text{ \AA}$ , and the TiO band-heads at  $\lambda\lambda 6647, 6676, 6711,$  and  $6742 \text{ \AA}$ . Days from the peak of the microlensing event are indicated along the vertical axis.

Fig. 14.— Same as Figure 13, showing the spectra divided by the median combination of all. These have been displaced in the vertical direction and arbitrarily scaled, such that the flattest spectra here actually display the largest range of excess from the median combination. Note the changes in  $H\alpha$  and the TiO bands in the two spectra nearest peak magnification.

Fig. 15.— Temporal evolution of the equivalent width in  $\text{\AA}$  of  $H\alpha$  and the TiO band-heads, measured with respect to the local pseudo-continuum. The EW plotted in the right panel are the sum of the TiO bands at  $\lambda\lambda 6647, 6676, 6711,$  and  $6742 \text{ \AA}$ .

Table 1. Global Microlensing Alert Network

Observatory	Latitude, Longitude	Aperture	Detector	Plate Scale ("/pixel)
MSO <sup>a</sup>	149 ° 00.5 <sup>m</sup> E , 35 ° 19.2 <sup>m</sup> S	1.27 m	8 x 2048 x 2048 Loral	0.63
CTIO <sup>b</sup>	70 ° 48.9 <sup>m</sup> W , 30 ° 30.9 <sup>m</sup> S	0.9 m	1024 x 1024 Tektronics	0.40
MJUO <sup>c</sup>	170 ° 27.9 <sup>m</sup> E , 43 ° 59.2 <sup>m</sup> S	0.61 m	1536 x 1024 KAF1600	0.23
UTSO <sup>d</sup>	70 ° 42.0 <sup>m</sup> W , 29 ° 00.5 <sup>m</sup> S	0.61 m	512 x 512 Photometrics	0.45
WISE <sup>e</sup>	34 ° 45.8 <sup>m</sup> E , 30 ° 35.8 <sup>m</sup> N	1.0 m	1024 x 1024 Tektronics	0.70

<sup>a</sup> Mount Stromlo Observatory, Canberra, Australia.

<sup>b</sup> Cerro Tololo Inter-American Observatory, Cerro Tololo, Chile.

<sup>c</sup> Mount John University Observatory, Lake Tekapo, New Zealand.

<sup>d</sup> University of Toronto Southern Observatory, Las Campanas, Chile.

<sup>e</sup> Wise Observatory, Mitzpe Ramon, Israel.

Summary of observatories participating in GMAN follow-up observations.

Table 2. MACHO Alert 95-30 microlensing statistics

Fit <sup>a</sup>	$t_0$ <sup>b</sup>	$\hat{t}$ <sup>c</sup>	$u_{\min}$	$u_*$	$\omega$ <sup>d</sup>
1	1321.2 (1)	67.70 (13)	0.04069 (12)	0	???
2	1321.2 (1)	67.36 (1)	0.05579 (1)	0.07335 (1)	22.1 (50)
3	1321.2 (1)	67.28 (27)	0.05408 (20)	0.07561 (9)	21.5 (49)

<sup>a</sup> Fit 1 is the best standard microlensing fit to the data, Fit 2 incorporates the extended size of the source star, and Fit 3 takes into account limb-darkening of the source.

<sup>b</sup> JD - 2448623.50.

<sup>c</sup> Einstein diameter crossing time.

<sup>d</sup> Lens angular velocity, relative to the source, is in  $\text{km s}^{-1} \text{kpc}^{-1}$  and assumes a  $61 \pm 12 R_{\odot}$  source at 9 kpc.

Comparison of event parameters between microlensing fits for MACHO Alert 95–30. Statistics are derived from simultaneous fits on all passbands. Reported uncertainties in the final significant digit(s) are the maximum extent of the surface in parameter space which has a  $\chi^2$  greater than the best-fit value by 1.

Table 3. MACHO Alert 95-30 microlensing statistics

Passband	# Observations	$\bar{d}m$ <sup>a</sup>	Fit 1 $\chi^2$	Fit 2 $\chi^2$	Fit 3 $\chi^2$
MACHO R	205	0.018	980.33	847.49	839.15
MACHO V	292	0.023	1069.65	964.16	963.86
CTIO R	103	0.019	307.58	124.97	126.51
MJUO R	41	0.019	184.56	46.68	42.62
UTSO V	55	0.020	101.34	48.64	50.28
UTSO R	96	0.013	488.20	82.91	90.09
WISE R	12	0.013	80.71	13.76	7.22
TOTAL	804		3212.40	2128.64	2119.76

<sup>a</sup> Average error, in magnitudes, for each passband.

Individual microlensing statistics for MACHO and GMAN observations of Alert 95–30. The number of constraints per passband for fits 1, 2, and 3 are four, five, and five, respectively.

Table 4. Photometry of the source star in MACHO 95-30

Observed	Extinction	Dereddened	Abs Mag, 8 kpc	Abs Mag, 9 kpc
$V = 16.21$	$A_V = 1.35$	$V_0 = 14.86$	$M_V = +0.34$	$M_V = +0.59$
$K = 9.98$	$A_K = 0.15$	$K_0 = 9.83$	$M_K = -4.69$	$M_K = -4.45$
$V - R = 1.39$	$E(V - R) = 0.34$	$V - R_0 = 1.05$		
$J - K = 1.12$	$E(J - K) = 0.23$	$J - K_0 = 0.89$		
$H - K = 0.26$	$E(H - K) = 0.08$	$H - K_0 = 0.18$		
$V - K = 6.23$	$E(V - K) = 1.21$	$V - K_0 = 5.03$		
Bolometric		$BC_K = -2.7 \pm 0.1$	$M_{\text{bol}} = -2.0$	$M_{\text{bol}} = -2.25$

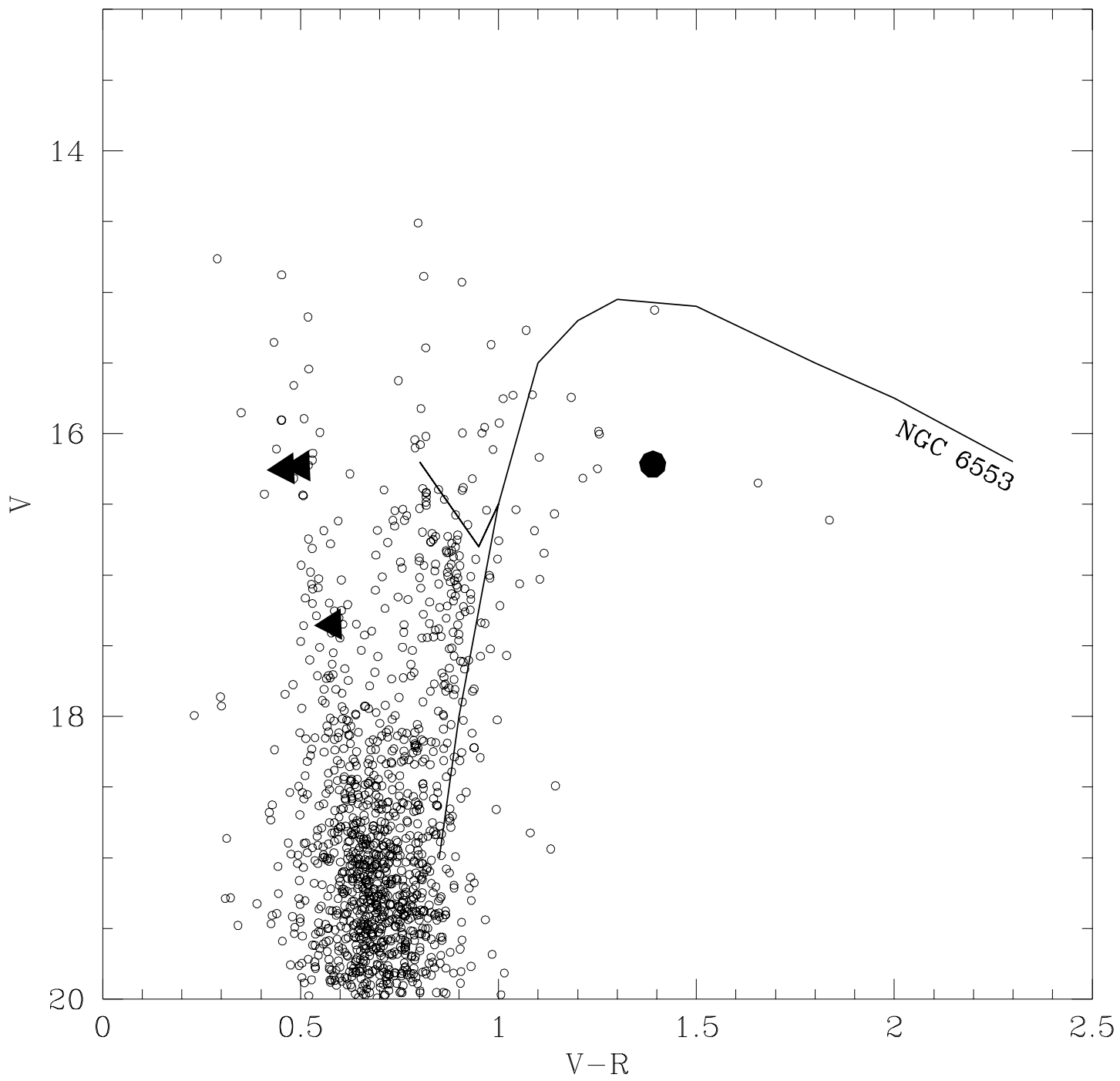
Table 5. Limb-darkening coefficients for the source star

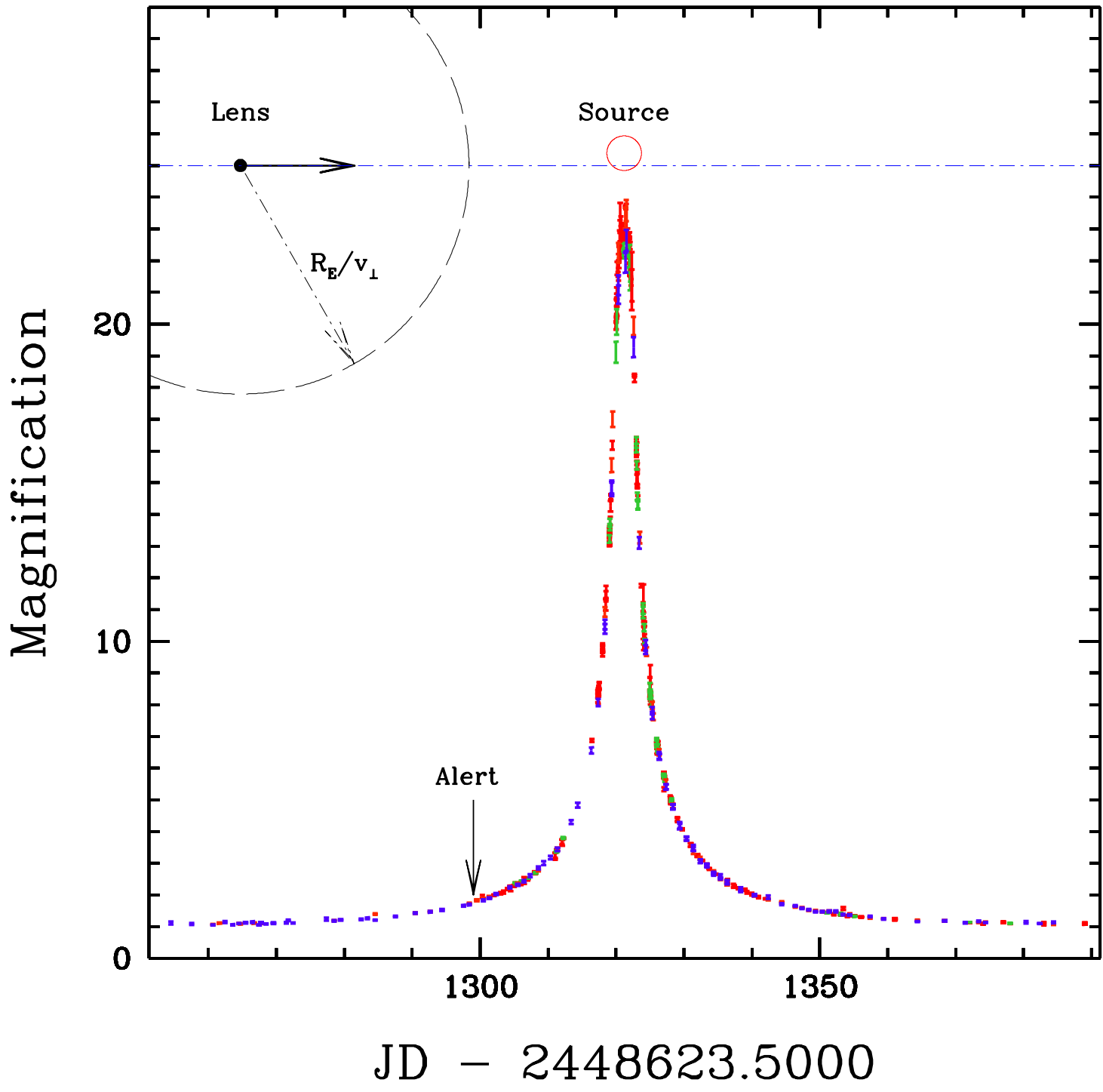
Passband	a	b
MACHO V	1.140	-0.284
MACHO R	0.825	-0.051
Standard V	1.072	-0.228
Standard R	0.910	-0.108

Limb darkening coefficients for Equation 3 used to approximate the brightness profile of the source star in MACHO Alert 95–30.

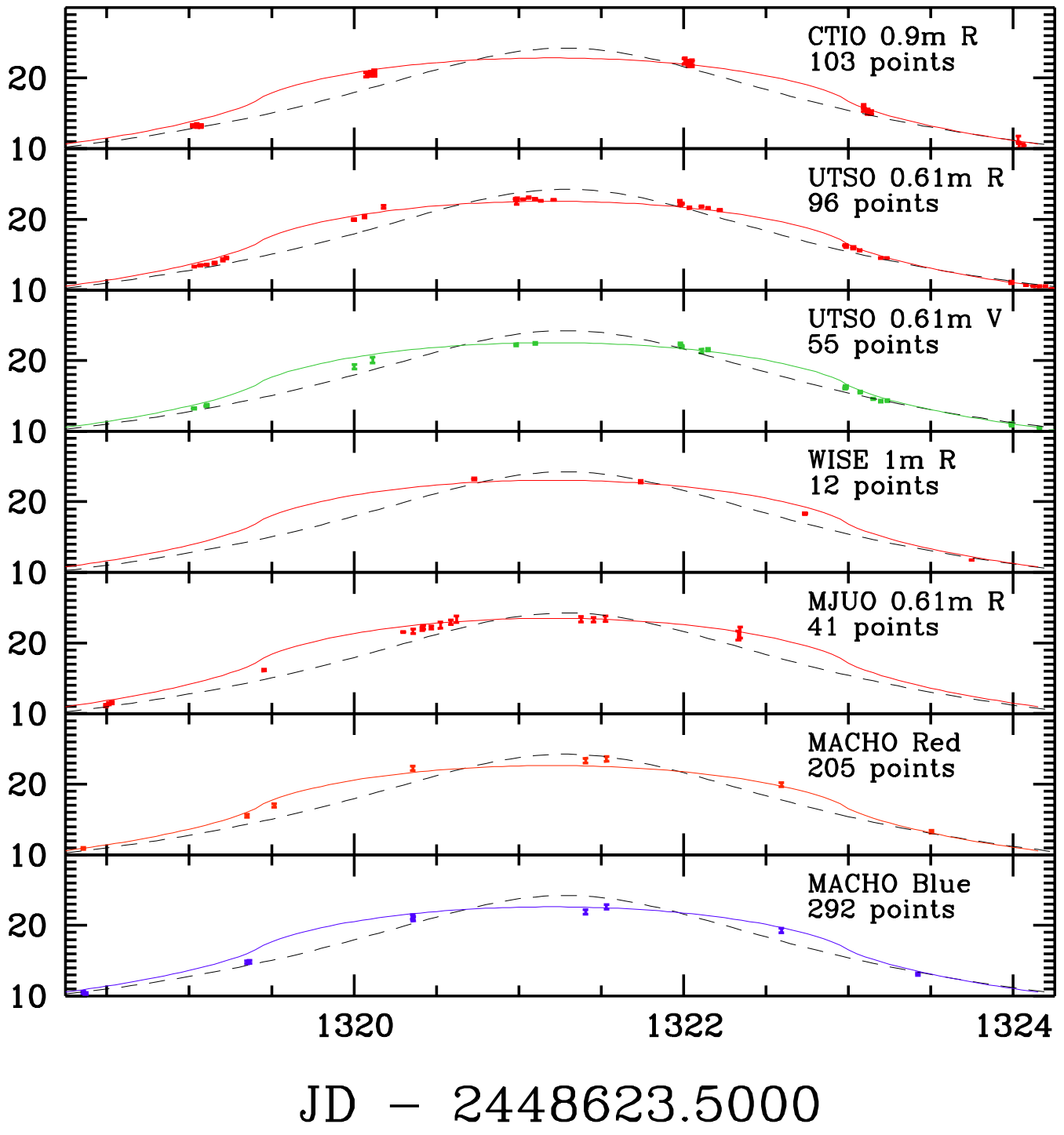
Table 6. Summary of spectral observations appearing in Figure 12

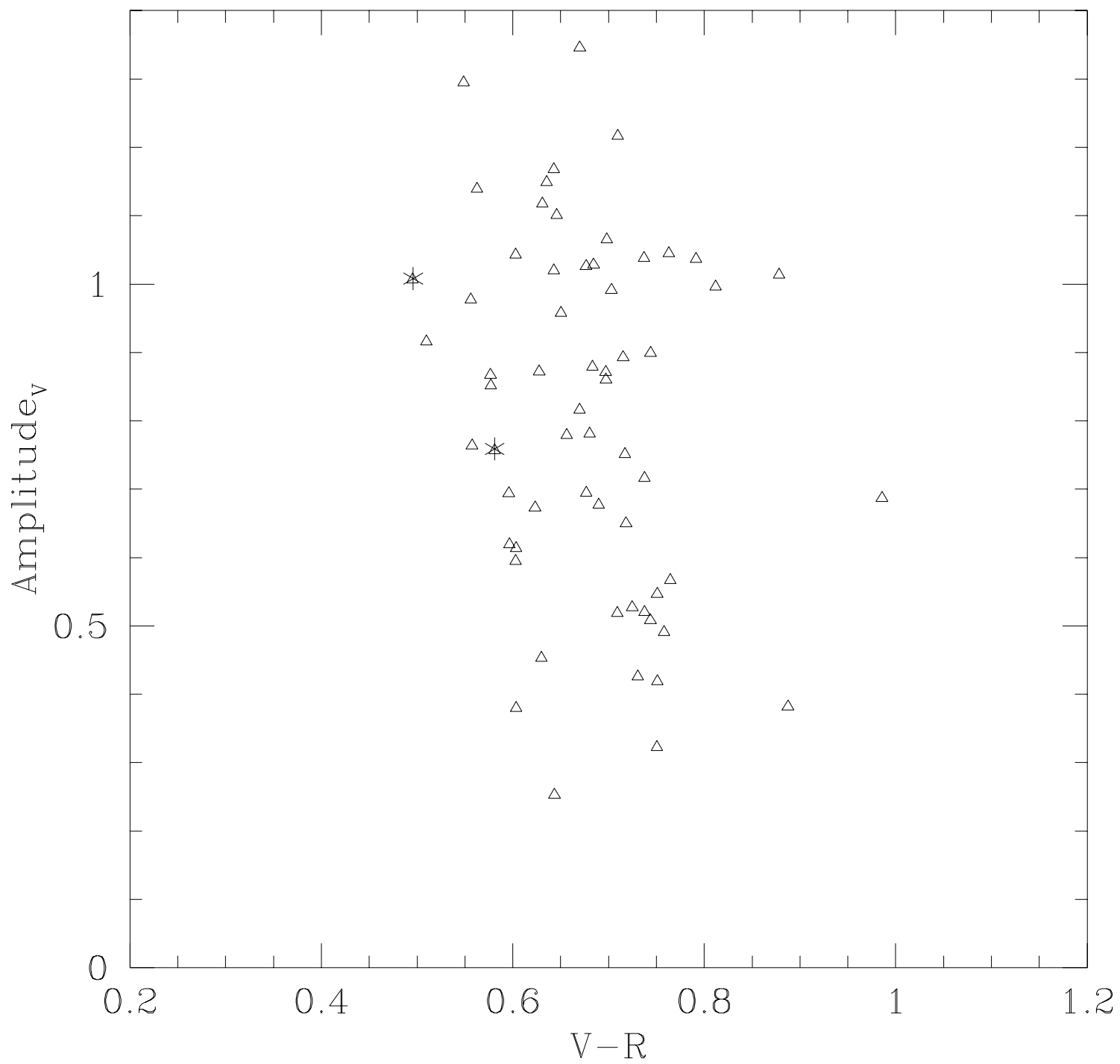
JD	Telescope & Instrument	Dispersion	Resolution	Coverage	S / N
2449944.234	CTIO 4m/RC Sp.	1.0 Å pix <sup>-1</sup>	4.0Å	6230–9340Å	~ 100
2449945.211	CTIO 4m/RC Sp.	1.0 Å pix <sup>-1</sup>	4.0Å	6230–9340Å	~ 100
2449947.221	Keck 10m/HIRES	0.04 Å pix <sup>-1</sup>	0.2Å	4309–6739Å	92-256
2449947.524	MSO 74"/Cass. Sp.	0.9 Å pix <sup>-1</sup>	4.6Å	6240–6770Å	106
2449948.223	Keck 10m/HIRES	0.04 Å pix <sup>-1</sup>	0.2Å	4835–7282Å	166-296
2449948.504	MSO 74"/Cass. Sp.	0.9 Å pix <sup>-1</sup>	4.6Å	6240–6770Å	117
2449949.509	MSO 74"/Cass. Sp.	0.9 Å pix <sup>-1</sup>	4.6Å	6240–6770Å	113
2449950.322	Keck 10m/HIRES	0.04 Å pix <sup>-1</sup>	0.2Å	3750–6065Å	20-141
2449950.523	MSO 74"/Cass. Sp.	0.9 Å pix <sup>-1</sup>	4.6Å	6240–6770Å	91
2449951.498	MSO 74"/Cass. Sp.	0.9 Å pix <sup>-1</sup>	4.6Å	6240–6770Å	96
2449952.508	MSO 74"/Cass. Sp.	0.9 Å pix <sup>-1</sup>	4.6Å	6240–6770Å	72
2449953.494	MSO 74"/Cass. Sp.	0.9 Å pix <sup>-1</sup>	4.6Å	6240–6770Å	78
2449954.513	MSO 74"/Cass. Sp.	0.9 Å pix <sup>-1</sup>	4.6Å	6240–6770Å	66
2449987.000	CTIO 4m/RC Sp.	2.0 Å pix <sup>-1</sup>	8.0Å	3890–9830Å	~ 100

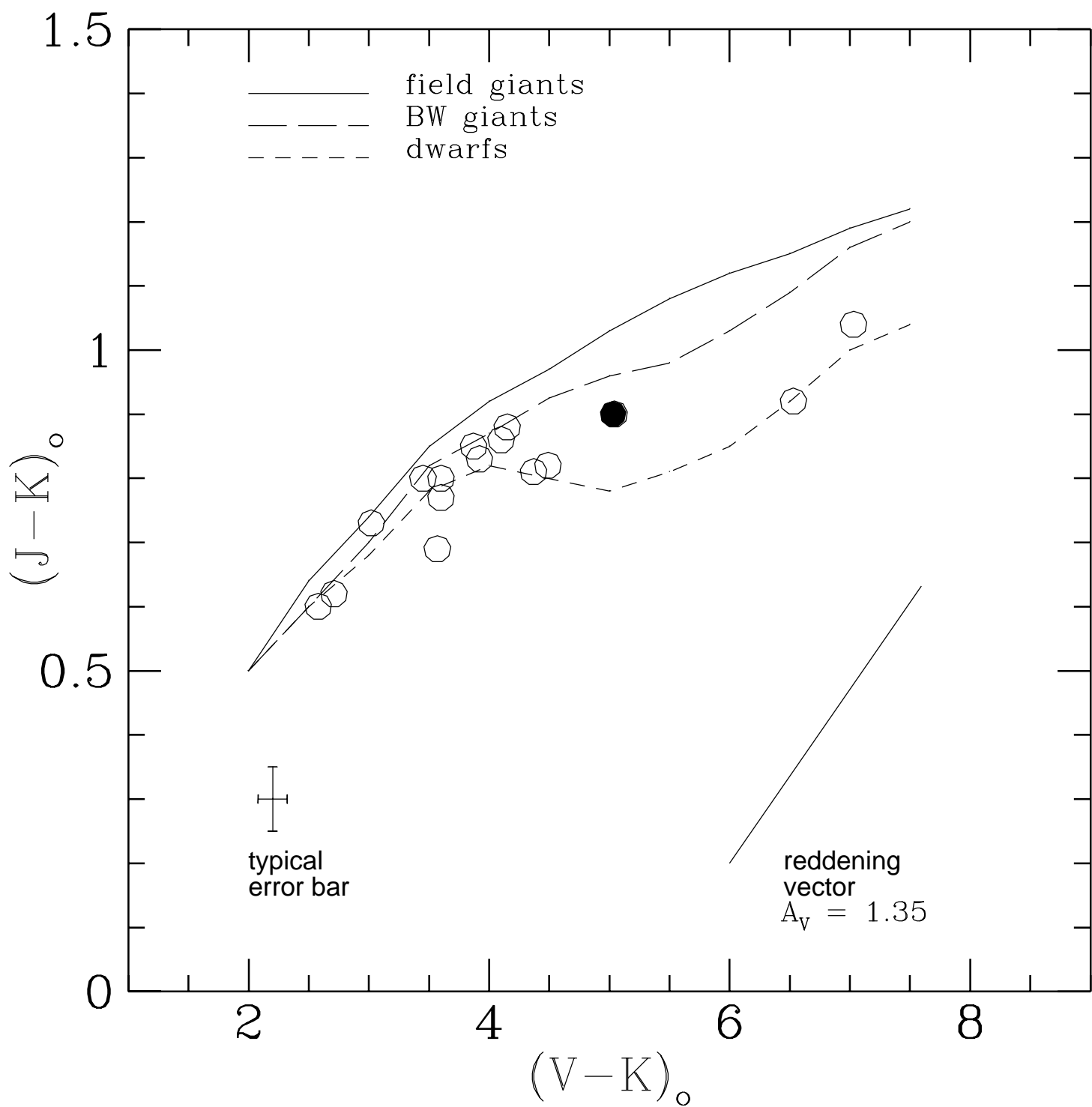


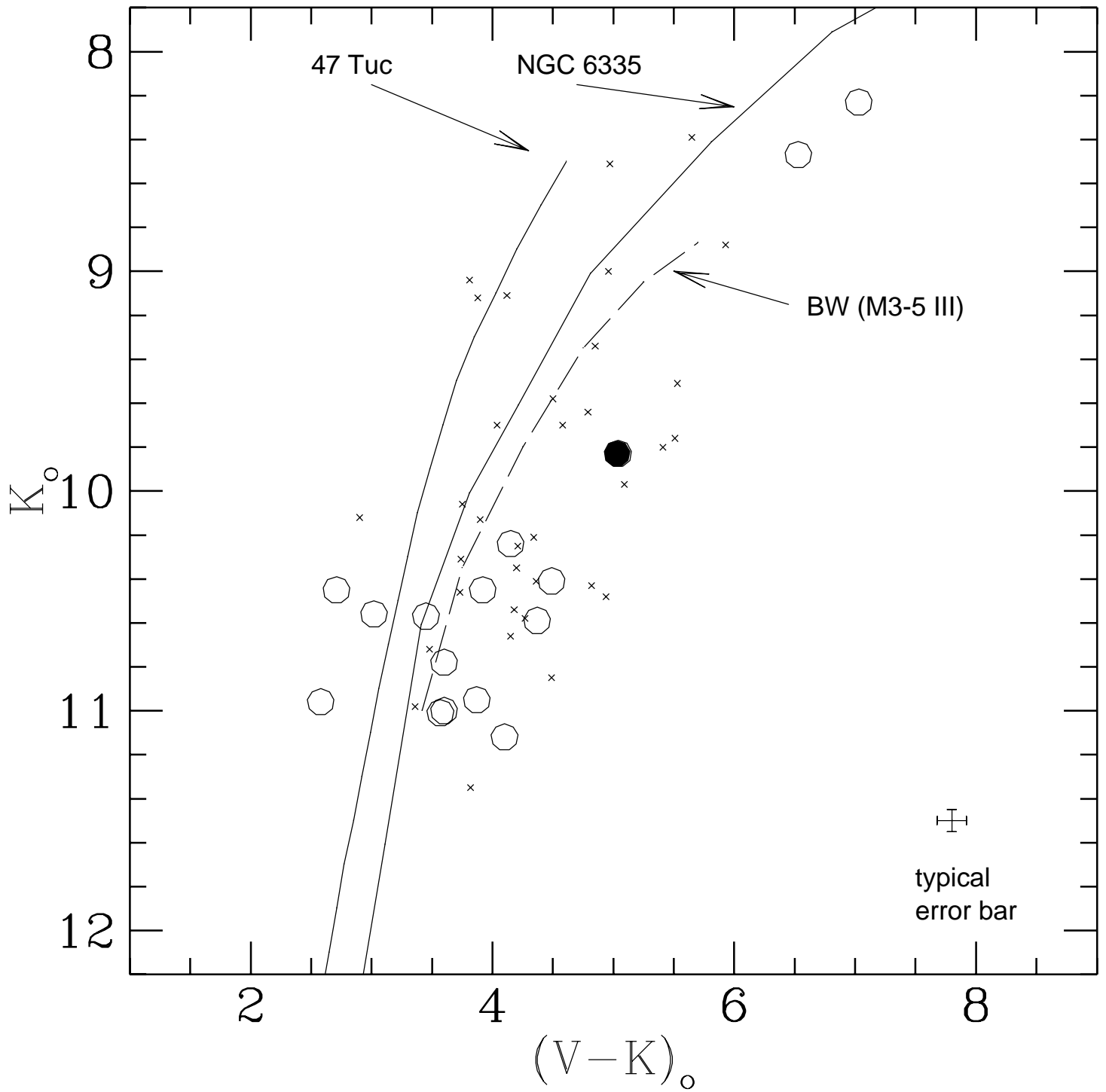


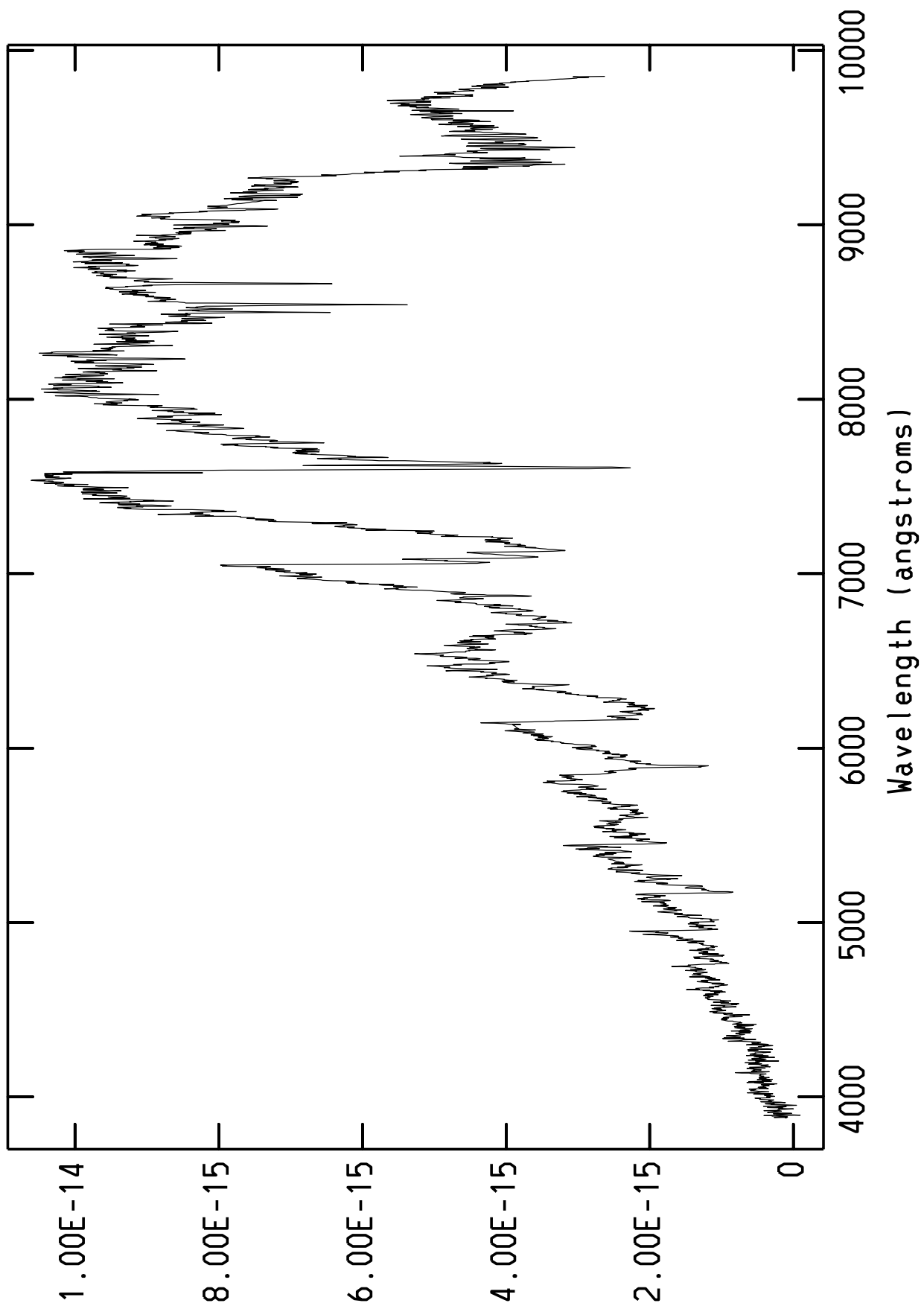
Magnification

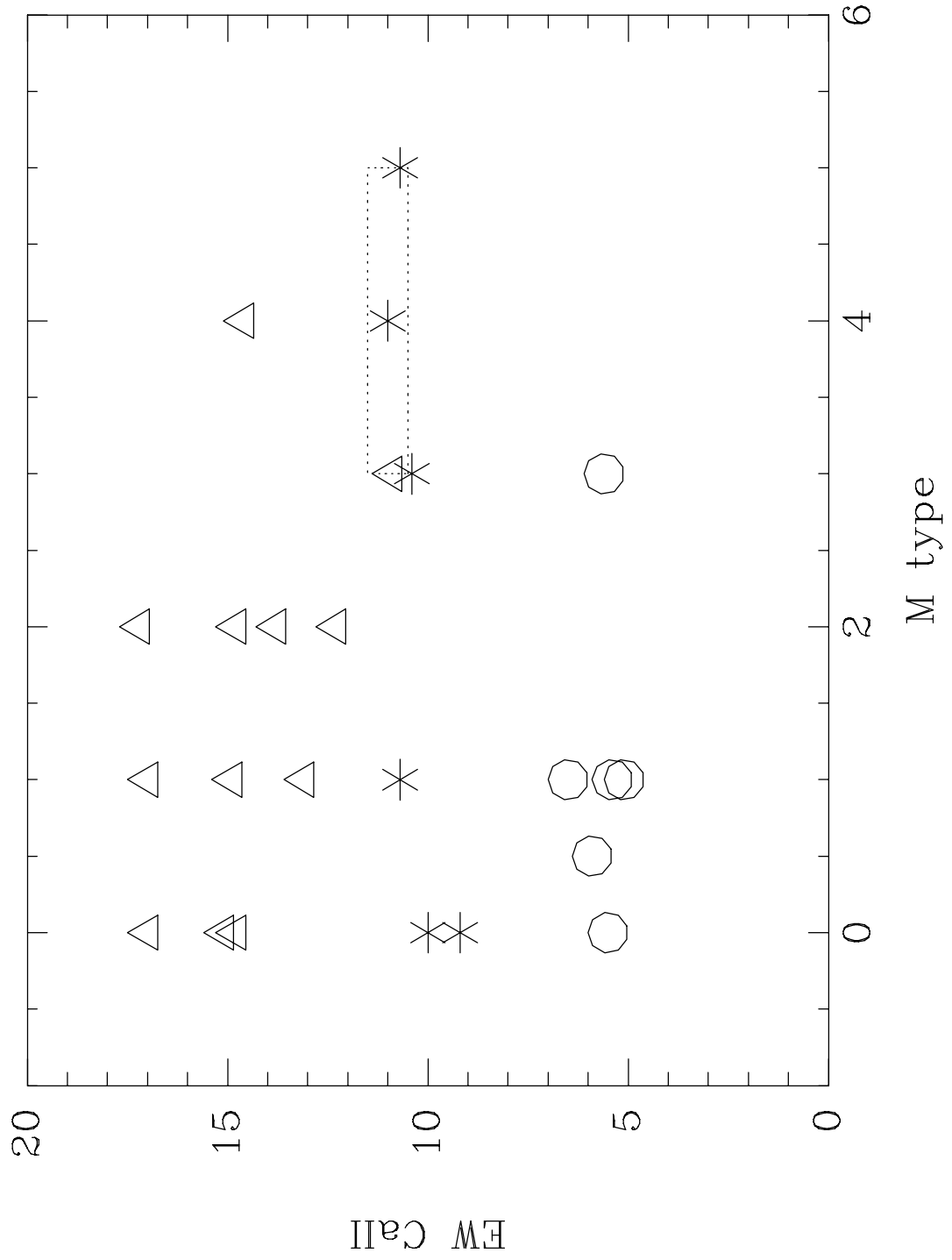




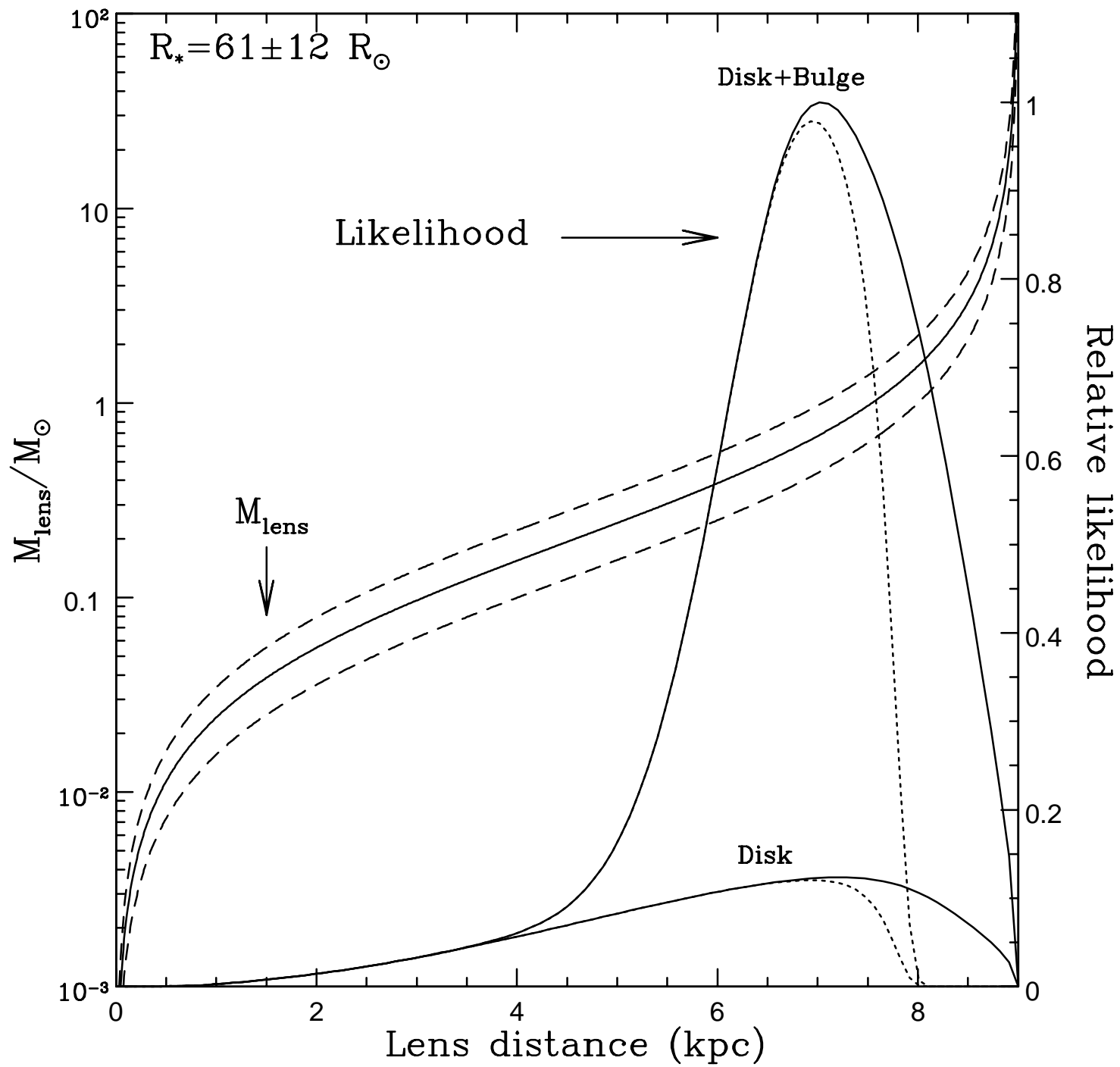


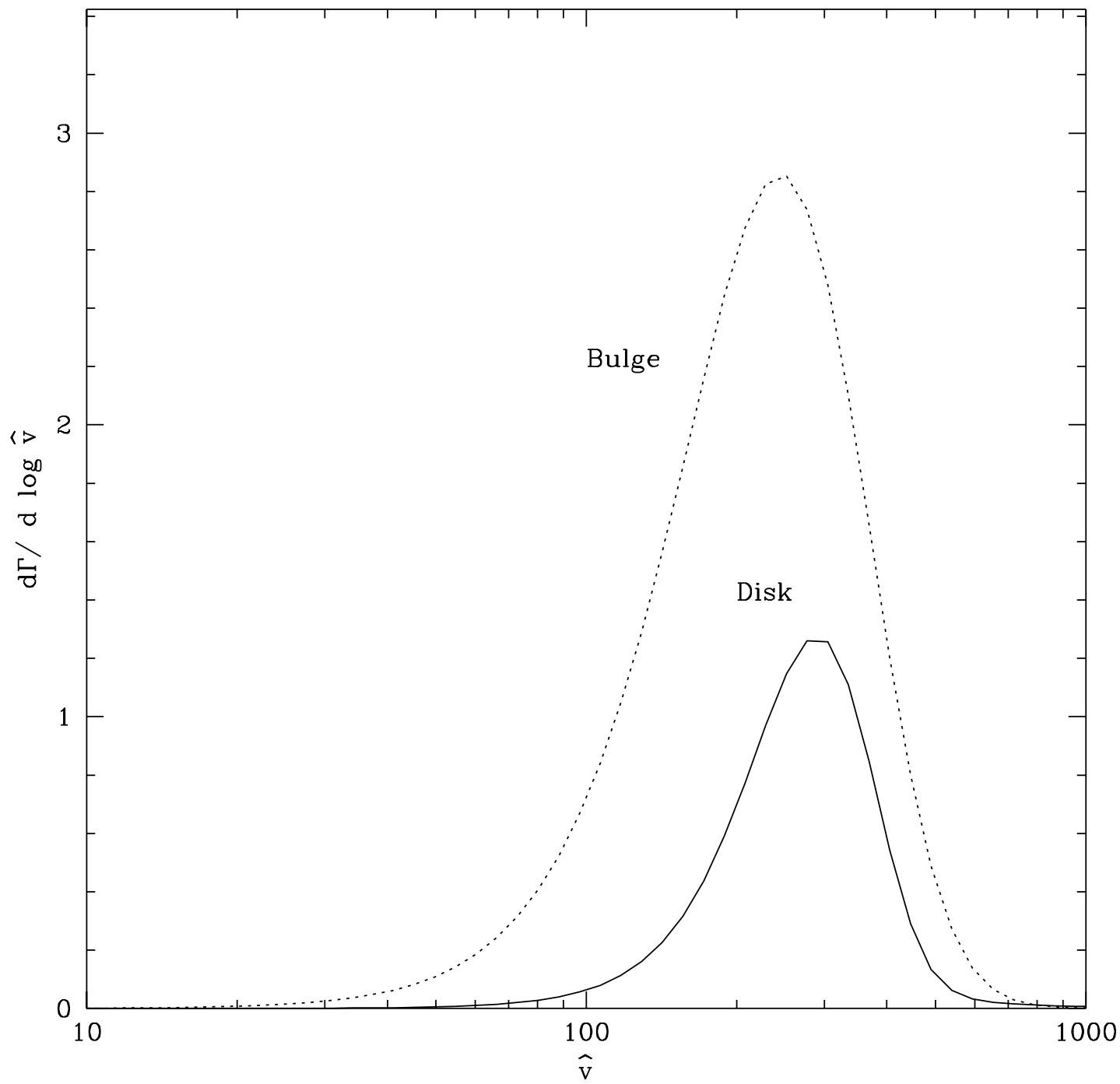


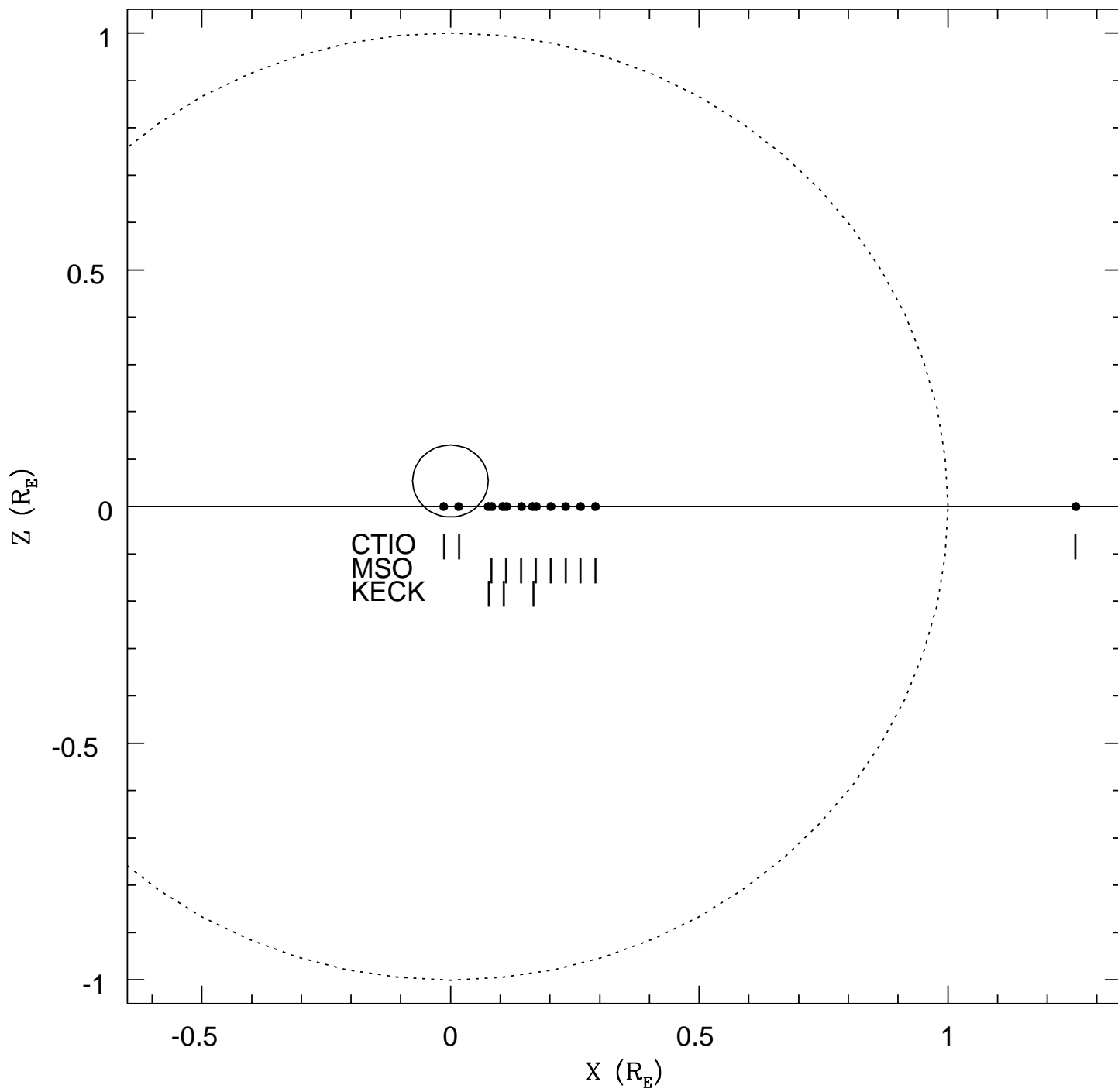




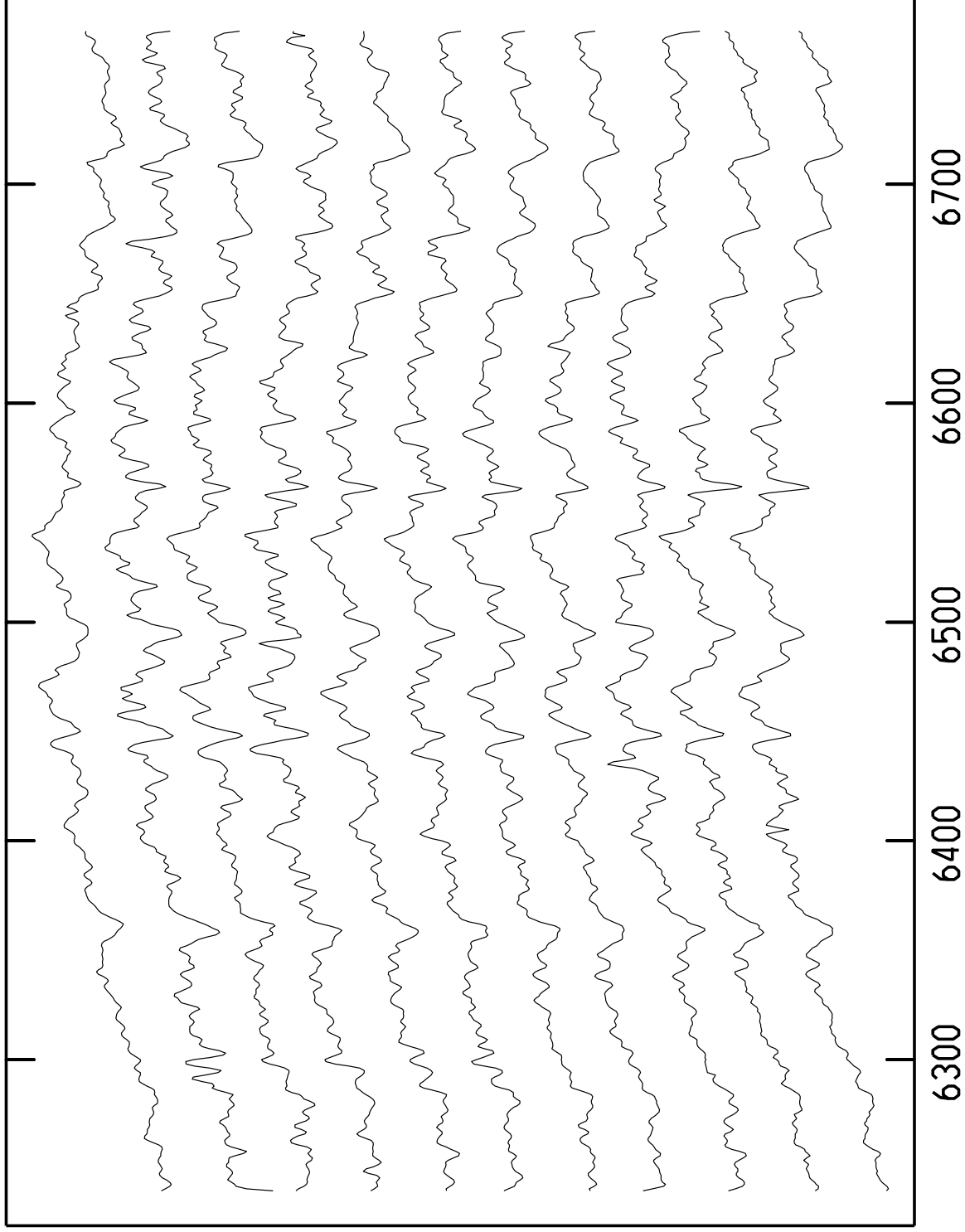




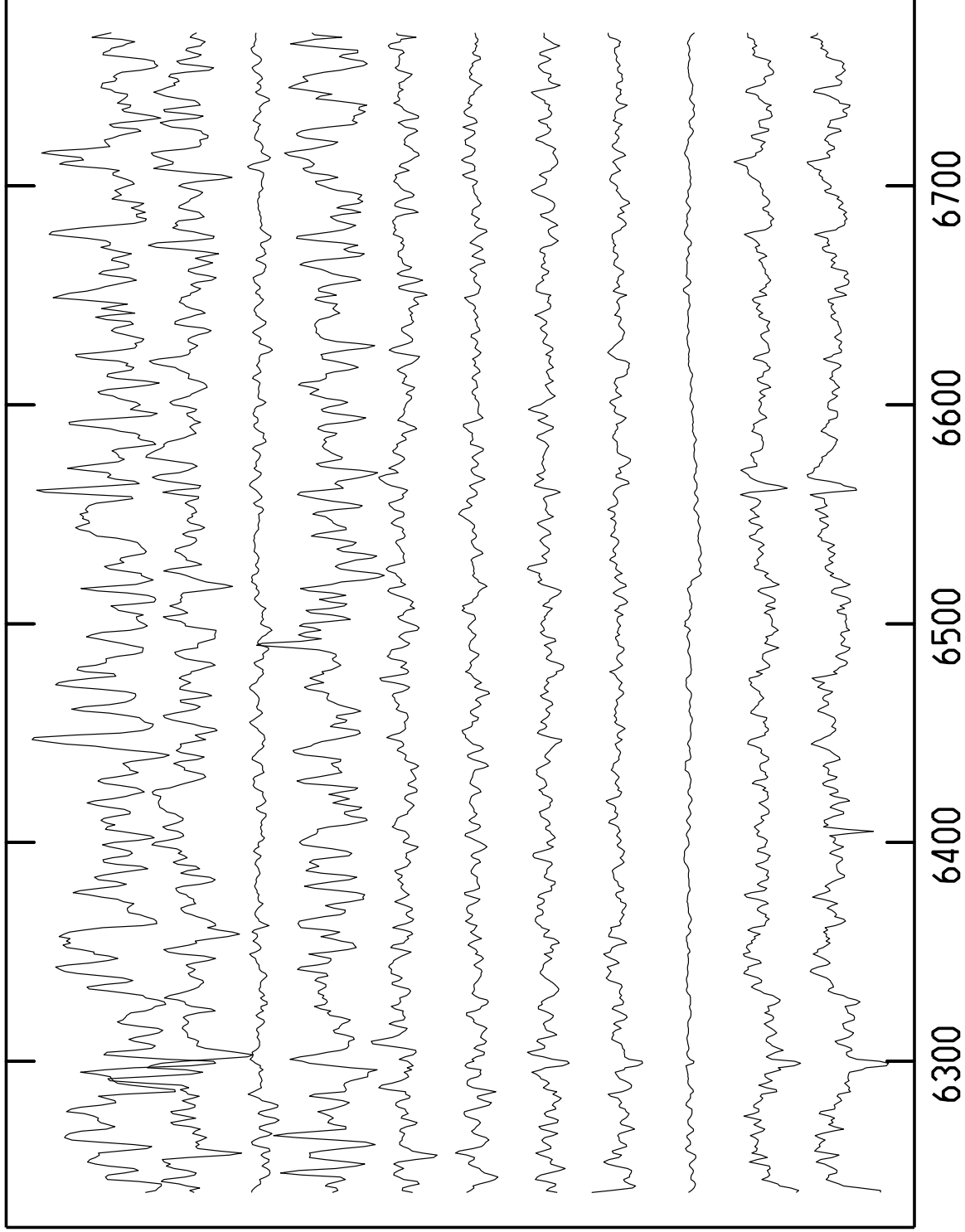




42.3 d  
9.8 d  
8.8 d  
7.8 d  
6.8 d  
5.8 d  
4.8 d  
3.8 d  
2.8 d  
0.5 d  
-0.5 d



Wavelength (angstroms)



42.3 d

9.8 d

8.8 d

7.8 d

6.8 d

5.8 d

4.8 d

3.8 d

2.8 d

0.5 d

-0.5 d

6300

6400

6500

6600

6700

Wavelength (angstroms)

